AGU
ADVANCING
EARTH AND
SPACE SCIENCES

JGR Planets

Key Points:

- During equinoxes, a nightside equatorial helium bulge is observed in NGIMS data, consistent with MarsPCM simulations
- MarsPCM predicted that helium bulges extend poleward and exhibit larger latitudinal extent than previously reported through a Martian year
- During peak of the Mars Year 34 Global Dust Storm, helium dispersed toward the dayside and restored its normal distribution during decay-phase

Supporting Information:

Supporting Information may be found in the online version of this article.

Correspondence to:
N. Gupta,
g.neha@uaeu.ac.ae

Author Contributions:
Conceptualization: Neha Gupta
Formal analysis: Neha Gupta, Bijay Kumar Guha, Shaikha Al Dhaheri, Piyush Sharma
Funding acquisition: Claus Gebhardt, Roland M. B. Young
Investigation: Neha Gupta, Bijay Kumar Guha
Methodology: Neha Gupta

Characteristics of Helium Bulges and the Impact of Martian Year 34 Global Dust Storm Using MAVEN/NGIMS Observations and MarsPCM and MGITM Simulations

Neha Gupta[1] [ID], **Bijay Kumar Guha[1]** [ID], **Claus Gebhardt[1,2]** [ID], **Shaikha Al Dhaheri[1,2]**,
Stephen Bougher[3] [ID], **Roland M. B. Young[1,2,4]** [ID], **Ehouarn Millour[5]** [ID], **Luca Montabone[5,6,7]** [ID],
N. V. Rao[8] [ID], and **Piyush Sharma[9]** [ID]

[1]National Space Science and Technology Center, United Arab Emirates University, Al Ain, UAE, [2]College of Science, Department of Physics, United Arab Emirates University, Al Ain, UAE, [3]Department of Climate and Space Sciences and Engineering, University of Michigan, Ann Arbor, MI, USA, [4]Department of Physics, SUPA, University of Aberdeen, King's College, Aberdeen, UK, [5]Laboratoire de Météorologie Dynamique (LMD/IPSL), Sorbonne Université, ENS, IPSL Research University, École Polytechnique, Institut Polytechnique de Paris, CNRS, Paris, France, [6]Centre for Mars Meteorology Monitoring, Le Bourget-du-Lac, France, [7]Space Science Institute, Boulder, CO, USA, [8]National Atmospheric Research Laboratory, Gadanki, India, [9]Physical Research Laboratory, Department of Space, Ahmedabad, India

Abstract We investigate spatiotemporal characteristics of helium (He) bulges using data from the Neutral Gas and Ion Mass Spectrometer aboard NASA's Mars Atmosphere and Volatile EvolutioN Mission and numerical simulations from the Mars Planetary Climate Model (MarsPCM). During equinoxes, we observed a He bulge at equatorial latitudes in addition to the mid-to-high latitude bulges reported in previous studies. This bulge is consistent with MarsPCM simulations. In addition, MarsPCM predicts a He bulge with larger latitudinal and poleward extents than previous studies suggest, persisting throughout the Martian year (MY) under nominal dust conditions. During equinoxes, the bulges span 85°N–90°S latitudes on the nightside. During solstices, the southern winter bulge is more dynamic between 0 and 8 hr local time (LT), and the northern one between 18 and 24 hr LT. Seasonal migration of He bulges occurs around solar longitudes (L_s) $\sim$ 50° and $\sim$183°, transitioning toward the winter hemisphere. We compare MarsPCM simulations using "climatology" and specific "MY 34" dust scenarios, alongside Mars Global Ionosphere Thermosphere Model (MGITM) simulations, to examine the impact of "MY 34" Global Dust Storm (GDS) during its pre-storm ($L_s \sim 184°$), peak ($L_s \sim 207°$), and decay ($L_s \sim 240°$) phases. Simulations indicate that the He bulge became most distorted during the storm's peak while remaining on the dayside. These distortions likely result from enhanced damping of meridional circulation at polar latitudes, contributing to the suppression of He bulges during high-dust seasons.

Plain Language Summary Helium, owing to its low mass, serves as a tracer for global circulation in Mars' upper atmosphere. Winds transport it and accumulate in convergence regions by downwelling, typically forming bulges in cold, nightside regions. Previous general circulation models predicted these bulges at mid-to-high latitudes in both hemispheres during equinoxes, and in the winter hemisphere during solstices, under typical Martian year conditions without an extreme, planet-encircling dust storm. However, this study reveals an additional bulge at equatorial latitudes during equinoxes. This demonstrates that helium bulges are consistently shifted to higher latitudes than previously predicted, persisting throughout the Martian year. Furthermore, this study utilizes the Mars planetary climate model and Mars global ionosphere thermosphere model to examine the effect of the extreme, planet-encircling dust storm during Martian Year 34 on helium bulge locations. We compare these simulations with those from a typical Mars year to isolate the impact of the storm during its different phases. The extreme, planet-encircling dust storm substantially reduces day-to-night circulation, resulting in helium being retained on the dayside. A plausible mechanism for this dampening of circulation involves storm-induced changes in the thermal and dynamical structure of Mars' upper atmosphere.

1. Introduction

Helium (He) is a noble gas that constitutes less than 1% of the Mars' atmosphere. Due to its low atomic mass and inert nature, it does not react with other atmospheric constituents and serves as a passive trace. In the upper atmosphere (>100 km altitude), diffusive separation causes He to become more abundant relative to heavier

species, as it has a larger scale height and responds more readily to vertical transport processes. These characteristics make helium a useful trace gas for studying global circulation patterns on Mars. The zonal and meridional winds, combined with vertical advection (upwelling and downwelling), lead to the accumulation of He in certain regions of Mars' upper atmosphere. These accumulated He density patches often appear as bulge-like structures, known as "Helium Bulges" (Bougher et al., 2015; Elrod et al., 2017; Gupta et al., 2021).

Vertical advection and molecular diffusion are the primary mechanisms driving the formation of He bulges on Earth (Liu et al., 2014). The horizontal winds only indirectly influence the process by maintaining thermospheric mass continuity. A similar mechanism is at play in forming He bulges on Mars (Aldhaheri et al., 2024; Bougher et al., 2015; Elrod et al., 2017, 2023; Gupta et al., 2021, 2024). On the dayside, the upwelling causes a decrease in He abundance relative to CO_2 density. Poleward-moving meridional winds carry He across the poles, converging on the nightside of Mars. Downwelling at the convergence point leads to the accumulation of helium, resulting in a significant increase in the helium-to-CO_2 ratio and the formation of He bulges (Bougher et al., 2015; Elrod et al., 2017, 2023; Gupta et al., 2021). Zonal winds play a crucial role in the local time (LT) variation of the Martian He bulges. They shift the convergence point of He to the morning and evening sides of the planet (Bougher et al., 2015; Elrod et al., 2017; Gupta et al., 2021). Additionally, the nightside convergence point exhibits a seasonal and latitudinal variation, migrating to higher latitudes in the winter hemisphere around solstices (Solar Longitude (L_s) ~ 90° and 270°). Gupta et al. (2021) and Elrod et al. (2017) reported the first observations of Martian southern (L_s ~ 90°) and northern (L_s ~ 270°) winter He bulges, respectively, at 180 km altitude, using the observations from the Neutral Gas and Ion Mass Spectrometer (NGIMS) (Mahaffy et al., 2014) aboard Mars Atmosphere Volatile EvolutioN (MAVEN) mission (Jakosky, Grebowsky, et al., 2015) spacecraft. During equinoxes (L_s ~ 0° and 180°), the nightside convergence point shifts to mid-latitudes in both hemispheres (Elrod et al., 2017; Gupta et al., 2021). These observations were compared with Mars Global Ionosphere Thermosphere Model (MGITM) simulations (Bougher et al., 2015; Elrod et al., 2017, 2023; Gupta et al., 2021). While MGITM simulations generally align with the observed seasonal variability of the He bulges (Elrod et al., 2017; Gupta et al., 2021), they consistently underestimate He bulge densities by 1–3 orders of magnitude (Gupta et al., 2021). Additionally, the model is not able to accurately capture the high-latitude nightside enhancements (>50°S) that are observed in NGIMS observations during equinoxes. These discrepancies are attributed to the absence of gravity wave (GW) parameterization in MGITM (Elrod et al., 2017, 2023; Gupta et al., 2021).

In late May to early June of 2018 (MY 34), a Global Dust Storm (GDS) enveloped Mars, marking one of the most substantially observed atmospheric events of the past decade (e.g., Felici et al., 2020; Guha & Panda, 2021; Guzewich et al., 2020; Montabone et al., 2020; Smith, 2019; Stcherbinine et al., 2020; Wolkenberg et al., 2020). Elrod et al. (2023) investigated the impact of the MY 34 GDS on the He bulge using NGIMS observations and reported a surprising decrease in the density of the northern winter He bulge. Their analysis focused on the early decay phase of the storm (L_s ~ 240°), where they compared MGITM simulated He density distributions and wind maps with NGIMS observations in detail. The simulations demonstrated that the dust storm can drive high-latitude He enhancements in the winter hemisphere. While He densities showed reasonable agreement between MGITM and NGIMS on the morning side (1–5 hr LT), significant discrepancies remained on the nightside (22–24 hr LT) at northern high latitudes (>50°N), where the model underestimated the observed densities. However, the simulated He distributions for the pre-storm (L_s ~ 184°) and peak (L_s ~ 207°) phases were presented only as line plots due to the lack of concurrent NGIMS He observations during those periods, making it difficult to directly compare model results with observations during the earlier stages of the storm. As a result, the evolution of He bulges across all phases of the MY 34 GDS has not yet been thoroughly examined using current general circulation models (GCMs).

While Gupta et al. (2021) utilized MAVEN observations spanning from MY 32 (L_s ~ 288°) to MY 35 (L_s ~ 230°), the present study extends the temporal range through MY 36 and into MY 37 (up to L_s ~ 207°). This broader data set provides enhanced coverage of seasonal and interannual variability in helium density. Notably, Gupta et al. (2021) excluded observations from L_s = 180°–360° during MY 34, during which time a GDS occurred. Elrod et al. (2023) on the other hand incorporated data from this period but focused solely on the early decay phase (L_s ~ 240) of the storm. In this study, we include the entire set of available NGIMS observations during the MY 34 GDS, enabling a more complete investigation of He variability across the pre-storm, peak, and early decay phases. This comprehensive approach not only improves the climatological context of He bulges but also facilitates a more robust comparison with He bulges during dynamically active periods of GDS.

This study has two primary objectives. First, we investigate the seasonal, latitudinal, and local-time variability of He bulges using NGIMS observations spanning MY 32–37, in conjunction with Mars Planetary Climate Model (MarsPCM) simulations. Previous studies have validated these variabilities exclusively through MGITM simulations, and no prior work has utilized alternative Mars GCMs such as the MarsPCM for this purpose. Consequently, persistent discrepancies between simulations and NGIMS observations remain unresolved. By incorporating MarsPCM, this study aims to provide a robust assessment of the He bulge morphology and variability, and to enable a more comprehensive understanding of the anomalous features identified in earlier analyses (Elrod et al., 2017, 2023; Gupta et al., 2021). Second, we examine the influence of the MY 34 GDS on He bulge evolution using MarsPCM and MGITM simulations. While earlier work (Elrod et al., 2023) has reported some effects of the storm on He distributions, the evolution of He bulges across the full lifecycle of the GDS including the pre-storm ($L_s \sim 184°$), peak ($L_s \sim 207°$), and decay ($L_s \sim 240°$) phases—has not been comprehensively studied using GCMs. Here, we address this gap by simulating He distributions across the pre-storm, peak, and decay phases of the MY 34 GDS using both models. Although direct validation is not possible for all intervals, these simulations provide critical insight into the dynamic response of the upper atmosphere to dust storm forcing. Here, we compare simulations using the MY 34's dust conditions with those from a nominal dust (climatology) condition within MarsPCM, enabling a robust assessment of the GDS impact.

Section 2 details the methodology used to process NGIMS observations and conduct simulations using the MarsPCM and MGITM models. Section 3 presents results on the spatial and temporal variability of He bulges using NGIMS observations and MarsPCM simulations of He densities. Section 4 examines the impact of the MY 34 GDS by analyzing MarsPCM and MGITM simulations during the pre-storm, peak, and decay phases. Section 5 discusses the combined results from Sections 3 and 4, highlighting the contributing factors to He bulge variability and the differences in parameterization schemes associated with the bulges in the two models. Finally, Section 6 summarizes the conclusions of this study.

2. Numerical Simulations and Observations

2.1. The Mars Planetary Climate Model

The MarsPCM is a 3-dimensional model of the Mars atmosphere, developed jointly by the Laboratoire de Météorologie Dynamique (LMD, Paris), the Instituto de Astrofísica de Andalucía (IAA), LATMOS, the University of Oxford, and the Open University (Forget et al., 1999). This model is supported by the European Space Agency and the Centre national d'études spatiales. MarsPCM simulates Mars' atmosphere from the subsurface to the exobase (~250 km), incorporating all significant physical and dynamical processes. The physical parameterizations for surface to lower atmosphere (~0–80 km), including subgrid-scale topography, boundary layer scheme, radiative transfer, CO_2 condensation, molecular diffusion, dust cycle, water cycle, and photochemistry, are detailed in Pottier et al. (2017), Navarro et al. (2014), Madeleine et al. (2011), and Forget et al. (1999). In recent years, several updates have been made to the model's physical parameterizations, including enhancements to the water and dust cycle, rocket dust storm representation, slope microclimates, and the convective boundary layer (Colaïtis et al., 2013; Forget et al., 2022; Gilli et al., 2020; González-Galindo et al., 2013; Lange et al., 2023; Lefèvre et al., 2008; Määttänen et al., 2022; Madeleine et al., 2011; Millour et al., 2024; Vals et al., 2022; Wang et al., 2018).

The upper atmosphere parameterizations, such as heating and cooling processes, Extreme Ultra Violet (EUV) radiative transfer, gravity wave drag, and ionospheric chemistry, are detailed in Gilli et al. (2020), González-Galindo et al. (2015, 2009, 2013), and Angelats i Coll et al. (2005). The non-orographic gravity wave (GW) parameterization, which was previously extended to ~100 km, has recently been extended up to ~250 km (Gilli et al., 2020; Liu et al., 2023). Additionally, the experimental setup including the number of vertical model layers has been updated from version 5 (Forget et al., 2022) to version 6 (Millour et al., 2024). While version 5 employed 49 vertical layers, the updated version 6 features 73 layers, providing higher resolution in the troposphere. However, the standard horizontal resolution remains the same between versions 5 and six of MarsPCM.

In this study, we employ MarsPCM version 5.0, configured with a horizontal resolution of 3.75° × 5.62° (longitude × latitude) using a hybrid sigma-pressure coordinate system. See the end of Section 5 for a discussion of why this study uses version 5.0 rather than version 6.0. The column dust optical depth (CDOD) in the model is prescribed with a "climatology" scenario (Montabone et al., 2015), derived by averaging dust opacity maps produced using observations during MY 24 to 35, excluding MY 25, 28, and 34 (Montabone et al., 2015, 2020).

This approach ensures that our simulations represent He climatology during typical Martian dust conditions, excluding periods of global dust storms. Additionally, to explore the effect of MY 34 GDS on these bulges, we run the model using the specific "MY 34" dust scenario (Montabone et al., 2020). Notably, we only use the simulations for growth ($L_s \sim 180°$), peak ($L_s \sim 207°$), and decay ($L_s \sim 270°$) phases of the GDS to compare with the simulations from MGITM (see Section 2.2). Finally, we use MarsPCM-simulated zonal and meridional winds from both the "climatology" and "MY 34" dust scenarios to examine changes in He bulges during the peak phase of the GDS. All simulations from MarsPCM shown in this study are analyzed at a pressure level of 1.38×10^{-6} Pa. At this pressure level, the absolute altitude varies between ~160 and 220 km over a Martian year (more details provided in Section 2.3).

The CDOD maps for MY 34 used in this work are derived from two versions of the Mars Climate Sounder (MCS) data set (version 5.2 and 5.3.2) aboard the Mars Reconnaissance Orbiter (MRO) (Montabone et al., 2020). In these dust maps, MCS data set version 5.3.2, only available for $L_s \sim 179–269°$ in MY 34, was an interim release incorporating the use of a far-infrared B1 detectors (at 32 μm), which extends dust profile retrievals deeper by 1–1.5 scale heights (Kleinböhl et al., 2017; Montabone et al., 2020). Additionally, improvements to surface temperature retrieval under high dust conditions enhance the accuracy of observations in cases where limb views do not reach the surface. These modifications are particularly useful for studying the impact of the MY 34 GDS through MarsPCM simulations using the latest available CDOD maps.

The MCS team has recently released a new version of their retrievals (version 6.2.1), which systematically uses the far-infrared B1 channel at 32 μm to extend the retrieved aerosol profiles into the lowest scale heights (Kleinböhl et al., 2024). These observations are currently being used to produce a new generation of CDOD maps, which not only incorporate updated observations but also improve the gridding methodology and the way observations from multiple instruments are combined. At present, this new version of the maps is still a work in progress, and could not be used in this study. However, as mentioned above, the maps for MY 34 already incorporate observations from the interim MCS version 5.3.2 during the GDS, which makes it unlikely that the future use of the new-generation maps would have a major impact on this study.

2.2. The Mars Global Ionosphere-Thermosphere Model

MGITM is a ground-to-exosphere (250 km) model (Bougher et al., 2015) adapted from the terrestrial Global Ionosphere-Thermosphere Model framework (Ridley et al., 2006). This model was developed to capture the compositional, thermal, and dynamical structure of the entire Mars atmosphere (~0–250 km). A state-of-the-art correlated-k radiation code is adapted from the NASA Ames Mars-GCM code (Haberle et al., 2003) to parameterize the lower atmosphere (~0–80 km) of Mars (Haberle et al., 1999). This code incorporates solar heating, aerosol heating, and CO_2 15-μm cooling. The dust inputs to MGITM were initially prescribed to be globally and seasonally averaged optical depth values using a Conrath parameterization for the vertical distribution (Elrod et al., 2017, 2020; Bougher et al., 2017; Bougher et al., 2015). This prescription served as a baseline preceding more sophisticated dust opacity data sets to be used. More recently, fully 2-D dust distributions have been empirically prescribed using vertical and horizontal data sets extracted from MCS (version 5.2.7) (Kleinböhl et al., 2009, 2011, 2017). Specific opacity maps were utilized to compute the MY 34 GDS aerosol heating rates within the MGITM code (Elrod et al., 2020; Jain et al., 2020). For the upper atmosphere, physical parameterizations are adopted from the Mars Thermosphere General Circulation Model, which includes EUV-UV heating, dissociation, ionization, CO_2 15-μm cooling, and ion-neutral chemistry (Bougher et al., 1999, 2000, 2015, 2023; Roeten et al., 2022).

Over the past decade, the MGITM code has undergone several significant updates, including those related to non-local thermodynamic equilibrium CO_2 15-μm cooling and EUV-UV fluxes. The current CO_2 15-μm cooling scheme is adapted from González-Galindo et al. (2013) and is also used for the construction of the MarsPCM code. The EUV fluxes are now incorporated from the Flare Irradiance Spectral Model, which is generated using solar flux observations from the EUV Monitor aboard the MAVEN spacecraft (Thiemann et al., 2017). Furthermore, the EUV neutral heating efficiency has been increased to 20% as suggested by Gu et al. (2020). Recently, a non-orographic GW parameterization code was adapted from Yiğit et al. (2008) for Mars and integrated into MGITM by Roeten et al. (2022). Standard gravity model parameters utilized in Roeten et al. (2022) are based upon commonly used values in previous Martian general circulation modeling studies of gravity propagation and dissipation (Medvedev et al., 2013; Shaposhnikov et al., 2022).

In this study, we focus on MGITM-simulated He densities for three specific phases—pre-storm, peak, and decay ($L_s \sim 184°$, 207°, and 240°, respectively)—of the MY 34 GDS, as well as MY 33, which represents a suitable He climatology for MGITM usage (see below). These simulations are specifically analyzed at an altitude of $\sim$200 km in the context of MGITM and MarsPCM model comparisons. MGITM typically runs on a $5° \times 5°$ regular horizontal latitude-longitude grid with 2.5 km vertical resolution (corresponding to 120 levels). Given the large-scale nature of He distribution in the Mars atmosphere, the slight differences in horizontal resolution between MGITM and MarsPCM simulations are not significant enough to alter the results of this study.

### 2.3. Neutral Gas and Ion Mass Spectrometer

NGIMS is an in-situ-based ion mass spectrometer onboard MAVEN (Mahaffy et al., 2014). The fundamental principle of operation of NGIMS is based upon quadrupole mass spectrometry, which separates atmospheric gases using their charge-to-mass ratio (Benna & Elrod, 2019; Mahaffy et al., 2014). NGIMS is designed to measure the abundances of major neutral species like CO_2, Ar, N_2, CO, O_2, O, N, He, etc., and major ionic species like CO_2^+, CO^+, O^+, H^+, etc. in the upper atmosphere of Mars (Benna & Elrod, 2019; Mahaffy et al., 2014). NGIMS operates in dual mode, alternating between a closed source neutral mode and an open source mode. In the closed source mode, the abundances of surface non-reactive species such as Ar, He, CO_2, and CO are determined. During open source mode, the instrument switches between neutral beaming mode and ion mode by keeping filaments off (Benna & Elrod, 2019; Mahaffy et al., 2014). The data retrieval pipeline to extract these abundances is detailed in Benna & Elrod, 2019. NGIMS has been operational since November 2014, providing observations of the Martian upper atmosphere above $\sim$160 km altitude, which is the spacecraft periapsis during the nominal science phase. Until 2018, MAVEN's periapsis during nominal observations was $\sim$160 km, except during deep dip campaigns when it was lowered to $\sim$125 km (Stone et al., 2018). Starting in August 2020, MAVEN's orbit was raised above $\sim$180 km altitude to support telecommunications with NASA rovers, and since then, its periapsis has remained between an altitude range of $\sim$180–220 km.

In the present study, we use He measurements from closed source mode by NGIMS from $L_s \sim 288°$ in MY 32 to $L_s \sim 207°$ in MY 37, covering a variety of latitudes and local times in each season. We use the Level 2-version 08-revision 01 data set for this study. Helium measurements from NGIMS are subject to some limitations, particularly at high altitude regions of the outbound leg of MAVEN's orbit, where the spacecraft ascends into regions of lower atmospheric density. To avoid such uncertainties, our analysis is confined to the inbound leg. Additionally, we exclude all observations before $L_s \sim 288°$, MY 32, due to uncertainties related to the instrument's filament settings. The exclusion of these data is consistent with the recommendation of Elrod et al. (2017). As the focus of this work is to investigate the horizontal variability of He bulges, we restrict our analysis to an altitude range of 175–225 km. This altitude range aligns with previous studies (Elrod et al., 2023; Gupta et al., 2021) and allows for a broader latitude and local-time coverage, ensuring consistency with previous studies. These observations are compared with MarsPCM simulations. To ensure a one-to-one comparison, the NGIMS data are averaged onto a 0.5 hr local time (LT) and 3.75° latitude grid. The large-scale height of He at these altitudes, also shown in Figures 2 and 5 of Mahaffy et al. (2015), minimizes vertical variability, allowing for a more focused examination of horizontal trends. This altitude range is within the altitude limits corresponding to the fixed pressure level utilized in the simulated outputs of both MarsPCM and MGITM.

3. Results

Figure 1 illustrates the LT versus latitude coverage of the MAVEN spacecraft corresponding to the He observations used in this study. All the data are divided into four distinct seasons in Figure 1. The four seasons presented here correspond to the cardinal L_s (centered at 0°, 90°, 180°, and 270°). Each season includes data between 175 and 225 km altitude and within ±45° of the cardinal L_s. For example, the data coverage shown in Figures (1a–1d), includes MAVEN's trajectory at L_s values ranging between 315–45°, 45–135°, 135–215° and 215–315°, centered around $L_s = 0°$, 90°, 180° and 270°, respectively.

During the northern spring equinox (hereafter NSE, $L_s = 0°$) and northern autumn equinox (hereafter NAE, $L_s = 180°$), as shown in Figures 1a and 1c, respectively, observations from MY 33 to 37 collectively provide reasonable coverage on both the dayside (8–18 hr LT) and nightside (0–8 and 18–24 hr LT) regions of Mars at southern mid-to-high latitudes (45–75°S). In addition, the observations from MY 32 further increase the data coverage during NSE. These data also provide an adequate LT coverage at mid- and low-latitudes (45°N–45°S),
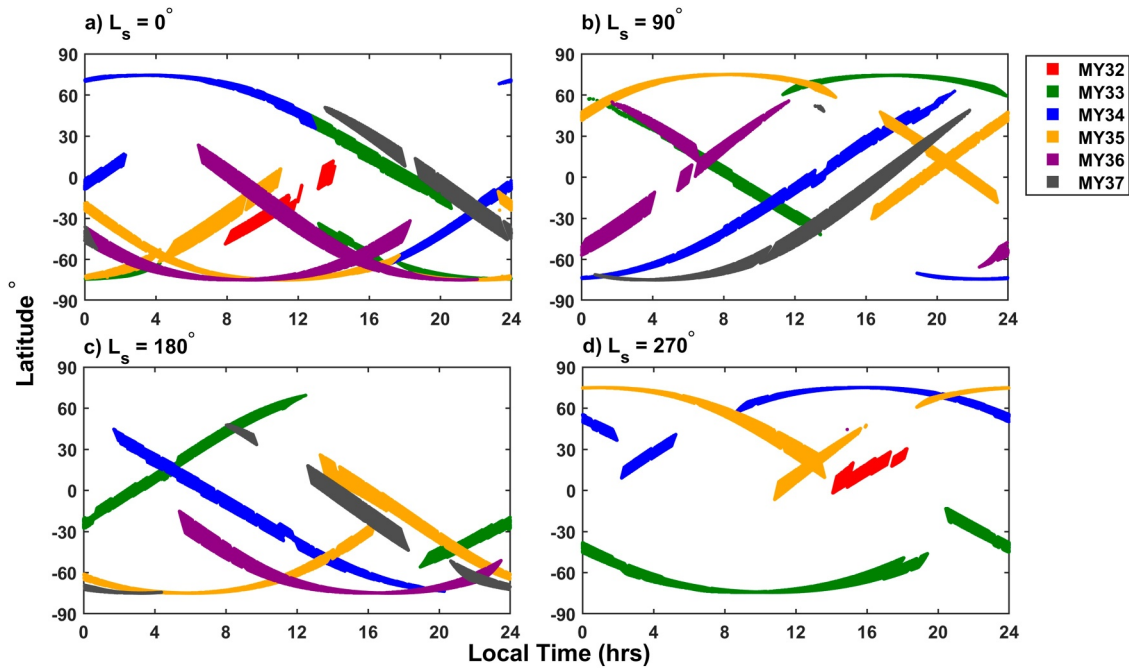
Figure 1. Latitude versus Local time distribution of MAVEN data coverage for panel (a–d) L_s 0°, 90°, 180°, and 270° as observed by NGIMS. The data shown here are for an altitude range of 175–225 km. Colors correspond to different Martian years.

except for a data gap between ∼2–6 hr LT during NSE (Figure 1a). Furthermore, during NSE, MAVEN data coverage at northern mid-to-high latitudes (45–75°N) is available between 0–13 hr and 23–24 hr LT in MY 34. However, during NAE (Figure 1c), data coverage at 45–75°N is sparse, primarily limited to local times between 8 and 13 hr on the dayside regions of Mars in MY 33.
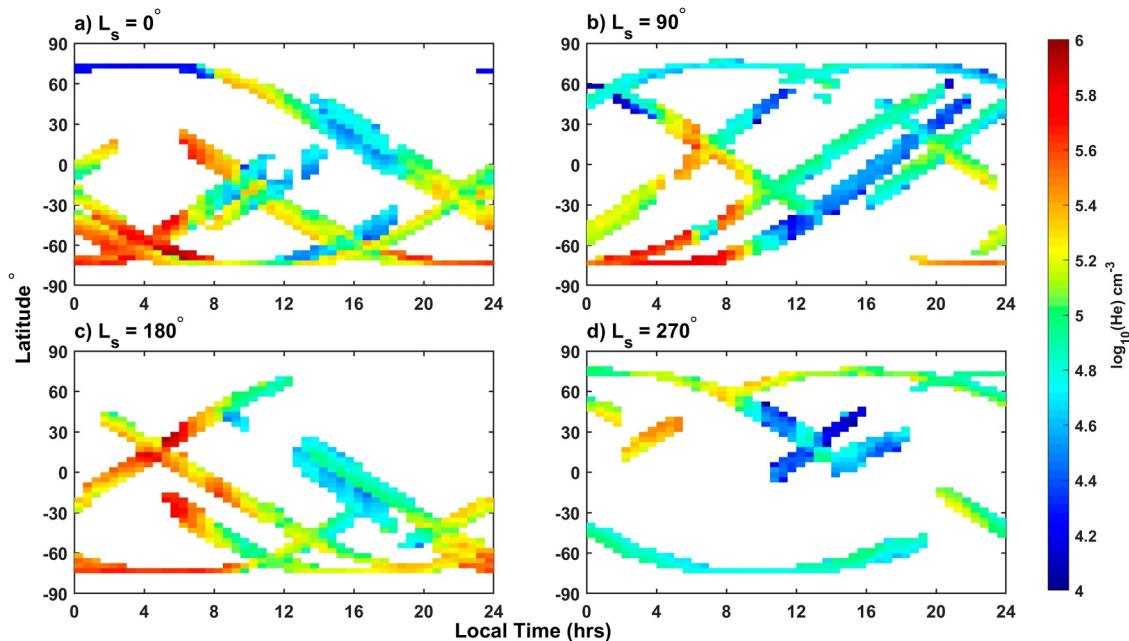
Figure 2. Same as Figure 1, but representing combined He densities in $\log_{10}$ scale for Martian years 32–37. The data are averaged on a local time and latitude grid of 0.5 hr × 5°.
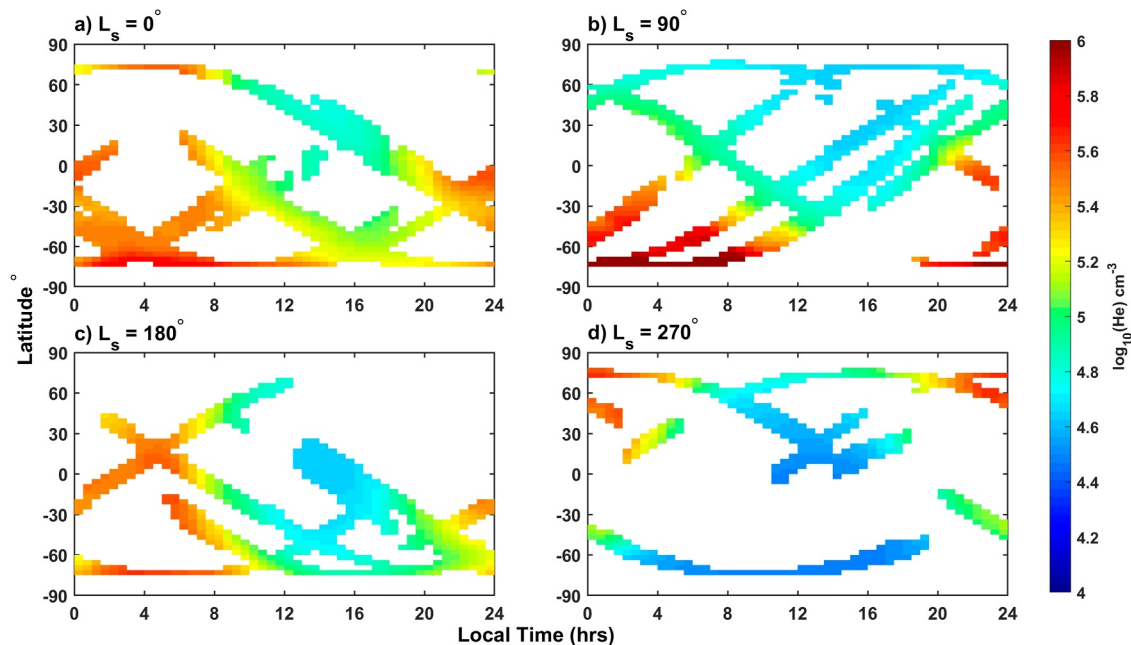
Figure 3. He densities from MarsPCM simulations with the climatology dust scenario at a pressure level of 1.38×10^{-6} Pa along the MAVEN trajectory for Martian years 32–37.

During the northern summer solstice (NSS, $L_s = 90°$; Figure 1b), MAVEN passed over southern mid-to-high latitudes during MY 34, 36 and 37, providing a reasonable coverage on the nightside regions of Mars. However, on the dayside only a few observations are available, mostly between 8 and 12 hr LT from MAVEN passes during MY 37 (see Figure 1b). MAVEN passes during MY 33 to MY 37 together provide adequate coverage at mid- and low-latitudes during most of the local times. Furthermore, MAVEN observed 45–75°N in MY 35 during 0–13 hr LT and in MY 33 during 12–24 hr LT, providing a continuous day-night coverage of the northern mid-to-high latitudes (Figure 1b).

During the northern winter solstice (NWS, $L_s = 270°$; Figure 1d), combined data from MY 32–35 provides marginal coverage at mid-to-high latitudes in both northern and southern hemispheres at most of the local times. However, data coverage at mid- and low-latitudes is sparsely available from MY 33–35 on the nightside and from MY 32 and 36 on the dayside regions of Mars. Moreover, the orbital trajectory of MAVEN provides adequate LT coverage in the NGIMS observations, particularly over the nightside convergence regions of helium, although it is not uniform across all latitudes.

The variability and data gaps observed across Martian years reflect the changing observational strategies and/or orbital configurations of MAVEN, such as deep dip campaigns and/or solar conjunctions (Jakosky, Grebowsky, et al., 2015). In addition, the orbital inclination of ~75° limits MAVEN's data coverage at polar latitudes (>75°) in both the northern and southern hemispheres. Moreover, there is ample coverage across all seasons, most local times, and latitudes, enabling a comprehensive understanding of the spatiotemporal variability of He bulges.

LT versus latitude variation of He densities for four seasons is shown in Figure 2. This figure is comparable to Figure 3 of (Gupta et al., 2021), but with a more extensive data set. During the NSE and NAE, the locations of He density enhancements and depletion are consistent with the previous studies (Elrod et al., 2017, 2023; Gupta et al., 2021). During NSE, expanded data coverage using MY 36 observations shows a density enhancement between ~20°N and 20°S from 5 to 9 hr LT. Despite a data gap between 2 and 5 hr LT, an increase in He densities is observed as MAVEN moves along its trajectory from ~10°S to 25°N between 3 and 4 hr LT. A similar enhancement was reported for the NAE, between 30°N and 30°S, in Gupta et al. (2021) and is also evident in Figure 2c. However, during NAE, there is a low-density patch extending from ~45°N to 20°S between 2 and 9 hr LT. This decreased density patch is likely due to the impact of the MY 34 GDS (Elrod et al., 2023). Moreover, during equinoxes, it is now evident that He densities increase not only at mid-to-high latitudes but also at equatorial latitudes (30°N–30°S).

By comparing Figures 2a and 2c, one can see a local time asymmetry in the southern hemisphere He bulge densities during both the NSE and NAE. The bulge densities between 18 and 24 hr LT are consistently weaker than those observed between 0 and 8 hr LT. While such an asymmetry was previously reported for NSE (e.g., Gupta et al., 2021), our study presents the first identification of this feature during NAE, made possible by incorporating additional data from MY 35–37, specifically, at ∼ 75°S. This pattern is also evident at mid-southern latitudes, where densities at ∼35–45°S (NSE) and 20–45°S (NAE) between 18–20 hr LT remain lower than those observed between ∼ 0–8 hr LT. These findings underscore the importance of extended temporal coverage in capturing subtle local time variations, particularly during NAE.

For the NSS, the observations from MY 37 (see Figure 1b) confirm the presence of a "southern winter bulge" at 45–75°S between 0 and 8, 18 and 24 hr LT (Figure 2b), which was previously observed using MY 34 observations (Gupta et al., 2021). In addition, the equatorial density enhancement at 10°S–30°N during 5–6 hr LT is observed. Interestingly, there is a region of decreased He density at 45°N–45°S between 12 and 23 hr LT. This data patch is from the NGIMS observations during MY 37 (as shown in Figure 1b). In contrast, adjacent to this patch, there is an increased density patch from MY 34 observations. During MY 37, Mars observed some infrequent regional or large-local dust storms between $L_s = 45°$ and $135°$, and at 45°N–45°S (Guha et al., 2024). The reduced density in this region may be attributed to the influence of those dust storms. However, similar storms occurred in other Mars years without producing a comparable depletion in densities. A comprehensive investigation of this phenomenon is beyond the scope of this study.

During NWS, a "northern winter bulge" is observed at 45–75°N between ∼0 and 8 hr LT (Figure 2d). As shown in Figure 1d, MAVEN observed the northern winter hemisphere during MY 34 and 35. Our analysis reveals that the nightside northern winter bulge around $L_s = 270°$ is nearly 10 times weaker than the southern winter bulge around $L_s = 90°$, suggesting a strong seasonal asymmetry. This asymmetry is also observed during 18–24 hr LT but with decreased magnitude. The northern winter He bulge was also reported using NGIMS measurements from MY 32 (Elrod et al., 2017). However, it is important to note that due to the high background noise in those observations, the bulge density was unusually low. Therefore, following this, we excluded these observations from our analysis, as discussed in Section 2.3. The densities are also enhanced at ∼10–45°N between 2 and 7 hr LT. While the southern winter bulge densities around ∼75°S between 0 and 8 hr LT are relatively higher than those during 20–24 hr LT, we do not observe significant local time asymmetry at ∼75°N during the NWS. To gain a deeper understanding of these observations, we compare NGIMS measurements with MarsPCM simulations of He bulges.

Figure 3 presents He bulge density from MarsPCM simulations prescribed with the "climatology" dust scenario at a pressure level of approximately 1.38×10^{-10} Pa for four seasons. The resolution of these simulations is similar to that of the NGIMS data. The simulations shown here are along the MAVEN trajectory over the same regions where NGIMS observations are available.

During equinoxes (NSE and NAE), the locations of mid-to-high latitude bulges on the nightside are consistent with NGIMS observations. However, during NSE, the MarsPCM simulated nightside bulge densities in the southern hemisphere are slightly lower than the NGIMS observed values (see Figures 2a and 3a). In contrast, the predicted densities on the dayside near ∼75°S are slightly higher than the observed values. Meanwhile, MGITM in Gupta et al. (2021) overpredicts the densities between 30 and 60°S on the nightside and underpredicts them at latitudes >60°S across all local times. For NAE, by comparing Figures 2c and 3c, one can see that the mid-to-high latitude density enhancement is almost accurately captured in the MarsPCM simulations. In contrast, MGITM in Gupta et al. (2021) underpredicts NGIMS observations (Gupta et al., 2021). Furthermore, the local time asymmetry observed in the NGIMS data is also evident in the MarsPCM simulations. The densities at most of the latitudes during equinoxes between 0 and 8 hr LT are higher than those between 20 and 24 hr LT. The nightside equatorial density enhancement during equinoxes is also well captured in MarsPCM simulations, although the densities are slightly underestimated. The most notable discrepancy occurs during NSE at ∼75°N on the nightside, where simulated densities are 1.2–1.4 times greater than the NGIMS observations. However, we cannot comment on this discrepancy conclusively as the observations in this region are insufficient and only available for MY 34. Moreover, the MarsPCM simulations predict an overall distribution of He bulges during the equinoxes that aligns more closely with NGIMS observations than other GCMs (Gupta et al., 2021). However, some discrepancies remain in the density magnitudes between the simulations and the observed data.
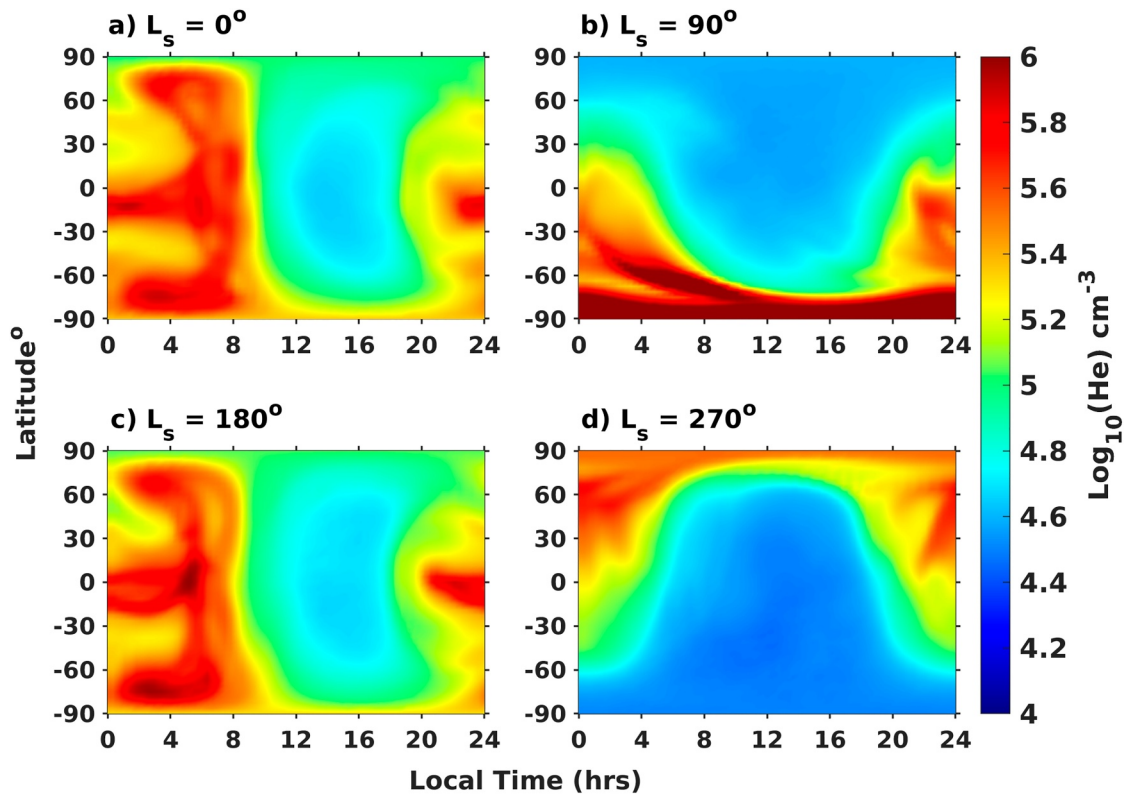
Figure 4. Same as Figure 3, but including simulation for all latitudes and LT.

During the solstices, the locations of the winter hemisphere He bulges in the simulations align well with NGIMS observations (Figures 2b and 2d) and previous studies (Elrod et al., 2017; Gupta et al., 2021). However, MarsPCM predicts higher He densities than those observed on the nightside during both solstice seasons. The most pronounced differences appear at mid-to-high latitudes in winter hemispheres, where simulated densities of He bulges are nearly an order of magnitude larger than those measured by NGIMS. During NSS, the density enhancement at 20–60°S between 0 and 6 hr LT is consistent with NGIMS observations. However, the simulated densities are slightly overestimated. Furthermore, the low-latitude density enhancements seen in NGIMS data between 4 and 8 hr LT are also apparent in the MarsPCM simulations, although the densities are slightly decreased. On the other hand, the dayside densities for solstices are underestimated at most of the latitudes, except for the density patch corresponding to MY 37, for which simulated densities are slightly higher than the observed densities (see Figures 1c and 2c).

Since the simulations shown in Figure 3 follow the MAVEN trajectory, our goal is to investigate the overall climatology of helium over a nominal Martian year, with a particular focus on regions not observed by MAVEN. This climatology is derived from MarsPCM simulations using a prescribed "climatology" dust scenario. Supplementary Movie S1 illustrates the day-to-day variations in He bulges under these nominal dust conditions, offering a comprehensive view of He distribution. MarsPCM simulations prescribed with the climatology dust scenario are detailed in Section 2.1. The day-to-day variation seen in Movie S1 is not strong enough to alter the broader characteristics of the He bulge; however, seasonal variation is. Therefore, a representative frame from the simulations, showing the He density distribution for each season, is presented in Figure 4. As mentioned previously, the simulations correspond to a pressure level of 1.38×10^{-6} Pa. At this pressure level, the corresponding altitude varies between 160 and 220 km. Within this altitude range, He exhibits very little vertical variation throughout the Martian year. Specifically, $\log_{10}(\text{He})$ varies only by about 0.4, implying an uncertainty in the MarsPCM simulations of ±0.2. Such uncertainty is negligible and unlikely to have a significant impact on the results of this study.
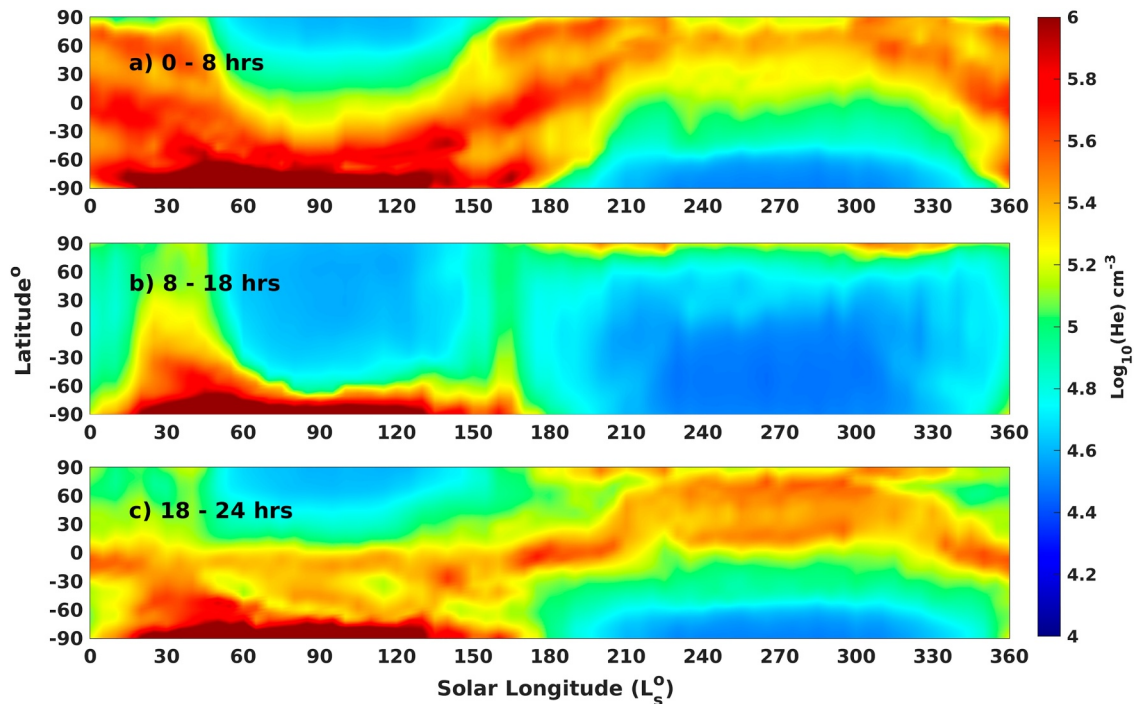
Figure 5. Zonal mean seasonal variation of the He density during local time intervals of (a) 0–8 hr, (b) 8–18 hr, and (c) 18–24 hr The data shown are from MarsPCM simulations with the "climatology" dust scenario at a pressure level of 1.38×10^{-6} Pa.

During equinoxes, He bulges are observed at most of the latitudes between 0 and 8 and 18–24 hr LT, with a strong presence at ∼ 45–90°N, 30°N–30°S, and ∼60–90°S between 0 and 8 hr LT. These locations of the bulges are consistent with previous studies (Elrod et al., 2017; Gupta et al., 2021). However, the bulges predicted by MarsPCM appear extended toward the higher latitudes than those predicted by MGITM (Elrod et al., 2017; Gupta et al., 2021). In MGITM simulations, He bulges are confined to 30–60° latitudes in both hemispheres, whereas MarsPCM predicts bulges that extend further toward the polar regions. In the southern hemisphere, during NSE and NAE, distinct bulges are observed between 60–90°S from ∼0 to 8 hr LT, with stronger magnitudes than their northern counterparts. As shown in Movie S1, this pattern is most clearly apparent between $L_s \sim 1°$ and $L_s \sim 25°$ for NSE and between $L_s \sim 156°$ and $L_s \sim 173°$ for NAE. Following these intervals, the asymmetry becomes slightly disrupted due to the seasonal shift of helium, although the latitudinal asymmetry persists until helium fully transitions to the winter hemisphere. A symmetric structure was evident in Gupta et al., 2021 and a deviation from that symmetric structure is visible around the equinoxes. On the nightside between 0 and 8 hr LT the southern He bulge near ∼90°S appears to extend from dayside toward nightside, suggesting a more global accumulation of He around the polar region. Additionally, bulge-like structures are seen at equatorial latitudes (30°N–30°S) during ∼4–7 hr and between 20 and 24 hr LT in both seasons. It is important to note that these equatorial bulges were not captured in MGITM simulations at any LT (Gupta et al., 2021). However, the equatorial He density enhancement observed in the NGIMS data aligns with MarsPCM predictions and suggests the presence of a nightside equatorial bulge during the equinoxes.

During NSS, He bulges are present in the southern hemisphere at latitudes ∼10–75°S between 0 and 8 hr and 20–24 hr LT, and from 75°S toward the southern polar region (90°S) extending to all the local times (Figure 4b). Conversely, the latitude and LT distribution of bulges during NWS is analogous to that observed during NSS, but in the northern hemisphere (Figure 4d). The southern winter bulge during NSS is ∼10 times stronger than the northern winter bulge during NWS, consistent with the NGIMS observations. Note that this seasonal asymmetry was not captured in MGITM simulations, which predicted bulges of equal strength (Elrod et al., 2017; Gupta et al., 2021).

Figure 5 represents the temporal evolution of He bulges over a typical Martian year. The data shown here include all the MarsPCM simulations that are shown in Movie S1. To better visualize the latitudinal and seasonal

asymmetry and migration of He bulges, the simulations are separated into three local time bins (0–8, 8–18, and 18–24 hr LT), as shown in Figure 5, where each panel shows the variation of He with solar longitude and latitude. The local time bins are based on local time variability of He shown in previous studies (Elrod et al., 2017; Gupta et al., 2021) and represent day and night boundaries at 8 and 18 hr LT. For clarity, the He bulges are further classified on the basis of their average density. In the following text, the portion of He bulges with average density $\geq 10^{5.6}$ cm^{-3} and $10^{5.4}$–$10^{5.6}$ cm^{-3} are termed as strong- and weak-bulges, respectively.

During NSE, a combination of strong and weak He bulges spans most of the latitudes in the nightside regions of Mars between 0 and 8 hr LT (Figure 5a). However, on the dayside (Figure 5b) and in the 18–24 hr LT bin on the nightside (Figure 5c), these bulges are restricted to the southern hemisphere latitudes. The strong bulge remains confined to the 60–90°S latitude range across all LT bins. The dayside bulges observed in the 8–18 hr LT bin (Figure 5b) are due to the southern polar region being on the nightside during this period. The weak-bulge begins to migrate toward the southern hemisphere around $L_s \sim 50°$ and remains concentrated on the nightside regions (0–8 and 18–24 hr LT) of Mars at 0–90°S until $L_s \sim 140°$. The strong-bulge does not show a migrating pattern. Then, during NAE, a weak-bulge is spread across most of the latitudes and is nearly equally extended on both sides of the equator between 0 and 8 hr LT. The bulge densities between 18 and 24 hr LT are significantly reduced across all latitudes. In the 8–18 hr LT bin, this weak bulge around NAE is primarily located between 60° and 90°S and near the north pole, with a continuous strip of bulge-like patches spanning all latitudes. This indicates the movement of the bulge from the southern to the northern hemisphere as Mars approaches the NWS, which is more prominent on the nightside of the planet. Around $L_s \sim 207°$, this bulge becomes entirely confined to the nightside northern latitudes (0–90°N). The weak-bulge remains confined to northern hemisphere until $L_s \sim 320°$ before repeating its seasonal cycle. In the 8–18 hr LT bin, the northern winter bulge becomes insignificant around the northern polar region, suggesting a strong presence of He bulges in the nightside winter regions of Mars throughout the year.

In addition, MarsPCM simulations show that the southern winter bulges during the 0–8 hr LT interval are more ubiquitous than those during the 18–24 hr LT interval (Figures 5a and 5c). For the 0–8 hr LT interval, a strong bulge extends from ∼45 to 90°S, whereas for the 18–24 hr interval, it extends from ∼65 to 90°S. In contrast, the latitudinal extent of the northern winter weak bulge during the 0–8 hr LT interval is smaller than that during the 18–24 hr LT interval. The key finding from this observation is that the latitudinal extent of the northern winter bulge is larger than that of the southern winter bulge, although the former is weaker than the latter. These findings were not evident in earlier simulations conducted by Elrod et al. (2017) and Gupta et al. (2021) using MGITM. It also suggests that the southern winter bulge is stronger during pre-midnight to post-dawn (0–8 hr), which becomes dusk to midnight (18–24 hr) LT for its northern counterpart. Also, it is evident that the dynamical behavior of the He bulges is more pronounced in the first half of the year ($L_s \sim 0$–180°) and during 0–8 hr LT compared to the second half of the year ($L_s \sim 180$–360°) and during 18–24 hr LT.

4. Effect of MY 34 GDS

4.1. MarsPCM Simulations

The MY 34 GDS event initiated on June 3 2018 ($L_s \sim 185°$) as a regional storm in southern Acidalia Planitia, which rapidly grew, merging with several local dust storms, and progressively intensified, eventually spreading across the entire planet (Shirley et al., 2020). On June 17 ($L_s \sim 194°$), this storm system marked the onset of a GDS. This GDS reached its mature phase between $L_s \sim 197°$–213°. The visible opacity (∼600 nm) observed during this period peaked between June 7 and 10 ($L_s \sim 207°$–208°) at a value of ∼9 (Kass et al., 2020). At this point, several thermal and compositional changes, associated with the dust storm were detectable in the upper atmosphere (120–250 km) of Mars (Chaufray et al., 2020; Elrod et al., 2020, 2023; Farahat et al., 2021, 2022; Jain et al., 2020; Liu et al., 2018; Venkateswara Rao et al., 2020). Dynamical processes such as global circulation and gravity waves were also altered (Leelavathi et al., 2020; Roeten et al., 2022; Yiğit et al., 2021). In addition, enhanced vertical transport of water associated with this GDS led to increased hydrogen escape rates (Heavens et al., 2018; Sun et al., 2023). Finally, the decay phase of the storm began around $L_s \sim 213°$ and continued until the dust opacity returned to its seasonal background level around $L_s \sim 280°$, allowing the atmosphere to resume its normal state.

Figures 6a–6c and 6d–6f illustrate the LT and latitudinal variations of He bulges from MarsPCM simulations, comparing the "climatology" scenario with a "MY 34" dust scenario for the pre-storm, peak and decay phases of
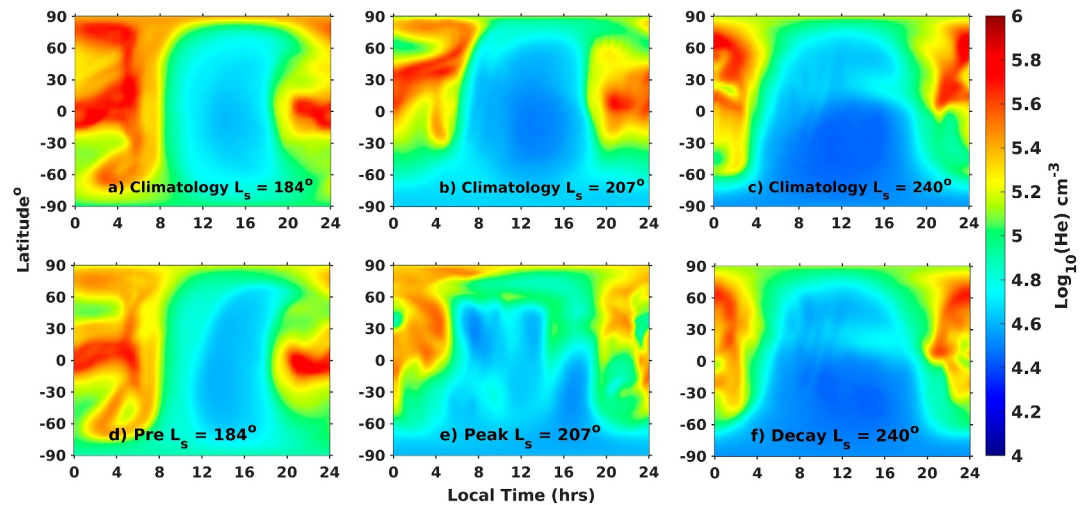
Figure 6. Latitude versus local time variation of the $\log_{10}$(He) density simulated from MarsPCM. The first column (a, d), middle column (b, e), and third column (c and f) represent data from the pre-storm ($L_s \sim 184°$), peak ($L_s \sim 207°$), and decay ($L_s \sim 240°$) phases of the MY 34 GDS. The top and bottom rows show the He densities from MarsPCM simulations with "climatology" and "MY 34" dust scenarios, respectively. All data shown here are at a pressure level of 1.38×10^{-6} Pa.

the GDS. During the pre-storm phase (Figure 6d), the LT and latitudinal patterns of He bulges closely resembled those observed in simulations with "climatology" scenario (Figure 6a). However, the bulge density is slightly depleted during the pre–storm phase for both the equatorial and high-latitude bulges. The decreased density patches in the He bulges make it appear mildly distorted. Also, the simulated He bulge with "climatology" scenario during 20–24 hr LT at equatorial latitudes (30°N–30°S) displays a conical shape that broadens as it approaches midnight (24 hr LT). However, during the pre-storm phase, the bulge's latitudinal width remains relatively the same throughout this LT.

MarsPCM simulation with "climatology" scenario shows the bulge at 10°S–90°N during ∼0–7 hr LT (Figure 6b). This location aligns with its characteristic tendency to follow the winter hemisphere as Mars transitions from the NAE to the NWS. However, during the peak phase of GDS, the bulge's strength is significantly reduced, and its location is slightly shifted (Figure 6e). Furthermore, simulations with "climatology" scenario indicate the presence of a He bulge at ∼ 10°S–45°N during ∼20–24 hr LT. In contrast, during the peak phase of GDS, a prominent bulge is absent; instead, a fragmented, weak bulge is dispersed across most of the hemisphere, excluding the southern polar latitudes. This weak and fragmented bulge observed during the ∼20–24 hr LT can be attributed to the overall enhancement in He density on the dayside (8–20 hr LT) of Mars. During the decay phase ($L_s \sim 240°$), MarsPCM simulations of He bulges with both "climatology" and "MY 34" dust scenarios (Figures 6c and 6f) exhibit nearly identical LT and latitudinal variations, except for a distorted density patch at 0–30°S during 22–24 hr LT in the MY 34 simulation. This indicates that during the decay phase of the GDS, He bulges tend to return to their nominal state. Additionally, MarsPCM simulations indicate that He bulges begin to re-establish their seasonal distribution around $L_s \sim 229°$. Although NGIMS data are available during the decay phase, limitations in temporal and spatial sampling prevent a direct one-to-one comparison with model outputs at all locations and times.

4.2. MGITM Simulations

Figure 7 presents MGITM simulations of He bulges comparable to the MarsPCM outputs shown in Figure 6. However, in this case, the He variability during a typical Martian year without a GDS is simulated using MY33 dust maps. MY33 experienced three regional dust storms between $L_s \sim 180$–330°, but lacked a GDS like the one in MY 34. Comparing He variability during the specific phases of MY 34 GDS with that of MY33 provides insight into the GDS's impact on He bulges. Hereafter, we refer to the MY33 simulations as the "climatology". MGITM predicted densities are approximately two orders of magnitude higher than those predicted by MarsPCM. This could be due to the differences in the dust gravity wave parameterizations in the two models. However, our focus
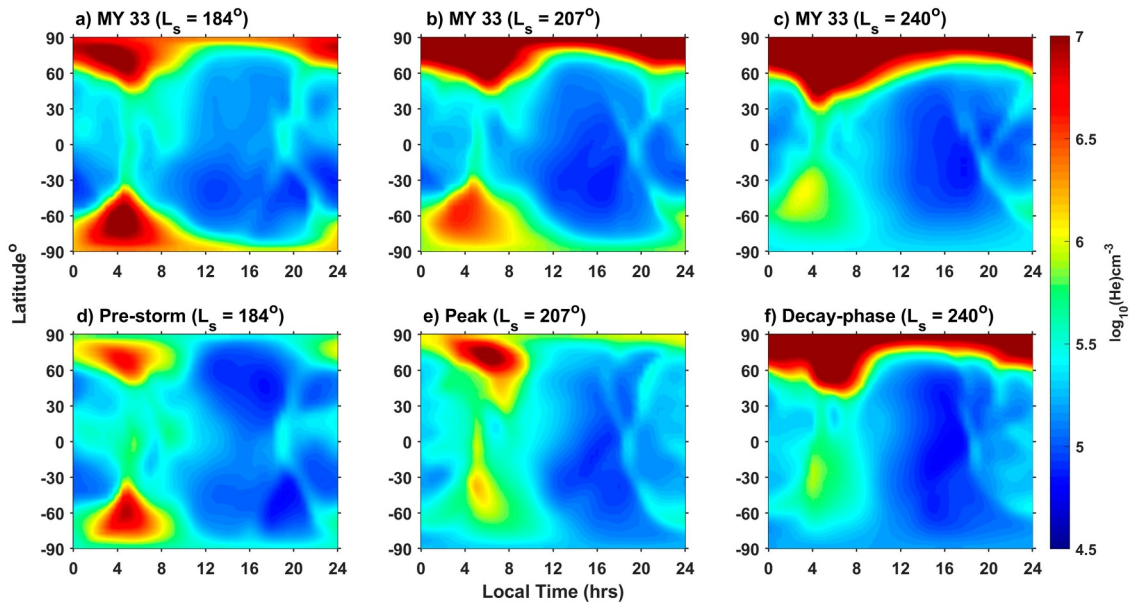
Figure 7. Similar to Figure 5, but representing He densities simulated from MGITM for MY33 in top row panels (a–c) and MY 34 in bottom row panels (d–f).

here is on the evolution of He bulges for different phases of the GDS; therefore, colorbars of Figures 6 and 7 are not kept identical to illustrate the variability.

The "climatology" simulations at $L_s \sim 184°$ (Figure 7a) show two He bulges between 0 and 8 hr LT at ~45–90° latitude in both hemispheres, extending to all local times at polar latitudes. The southern hemisphere bulge extends more equatorward than its northern counterpart, which is instead more elongated toward midnight. During the pre-storm phase (Figure 7d), both bulge densities decrease, particularly for the northern hemisphere bulge. A continuous patch of enhanced density appears between 0 and 12 hr LT at 0–30°N, which is seen as distinct patches in the "climatology" (Figure 7a). These locations and elongated He bulges in MGITM simulations with "climatology" and "pre-storm" dust scenarios (Figures 7a and 7d) align well with MarsPCM (Figures 6a and 6d) simulations, particularly the decrease in He bulge strength during the pre-storm phase of the MY 34 GDS.

In the MGITM "climatology" simulations during $L_s \sim 207°$ (Figure 7b), the local time and latitude distribution of He bulges is similar to that during $L_s \sim 184°$. However, the northern hemisphere bulge densities are notably higher for $L_s \sim 207°$ than for $L_s \sim 184°$, especially near the polar region across all local times. Conversely, the southern hemisphere bulge is weaker during $L_s \sim 207°$ than during $L_s \sim 184°$. This suggests a pronounced displacement of helium densities toward northern polar latitudes as the dust storm intensified. During the peak phase of GDS (Figure 7e), MGITM simulations show a distinct He bulge at 45–90°N during ~2–8 hr LT. The He density is significantly reduced at other local times compared to the "climatology" (Figure 7b). The southern hemisphere bulge is significantly weaker in magnitude and about 10 times smaller in size than in the "climatology" simulations, lacking a defined shape and dispersing toward lower latitudes between 4–8 hr LT. The dayside density enhancement, particularly between ~8 and 12 hr, resembles that in MarsPCM simulations (see Figure 6e), though MarsPCM shows more pronounced dayside scattering.

MGITM simulations for the early decay phase are detailed in Elrod et al. (2023). Here, we note that the northern hemisphere bulge during the decay phase (Figure 7f) is weaker but more confined within the nightside, which was disturbed during the peak phase (Figure 7e). Instead, its density is more comparable to the "climatology" simulations during $L_s \sim 240°$ (Figure 7c). In addition, He density distribution in northern hemisphere (Figure 7f) is similar to the "climatology" outputs for $L_s \sim 240°$ (Figure 7c). Overall, He density variability during the decay phase closely resembles the "climatology" outputs. Similar observations from MarsPCM suggest that the He bulge returns to its seasonal norm during the decay phase of GDS.

5. Discussion

He bulges in the Martian upper atmosphere have been extensively studied using both NGIMS observations and MGITM simulations (Bougher et al., 2015; Elrod et al., 2017, 2023; Gupta et al., 2021). During nominal dust conditions, the NGIMS observed bulge locations and their seasonal and temporal variability aligned with simulations from MGITM. However, significant discrepancies were observed, which are associated with the lack of GW parametrization in the model (Elrod et al., 2017, 2023; Gupta et al., 2021). During high dust conditions (MY 34 GDS), NGIMS observations during the decay phase of the storm ($L_s \sim 240–260°$) showed a decrease in bulge density. A GW updated version of MGITM further confirmed this decrease and reduced some of the data-model differences. However, discrepancies on the nightside at latitudes >50°N persisted (Elrod et al., 2023). In addition, the northern winter bulge simulated using this updated model was shifted further poleward from its previous locations. However, investigation of He bulge variability by comparison of NGIMS data through comparison of NGIMS observations with a gravity wave updated model under nominal dust conditions remains to be explored. In addition, the morphology of He bulges through the evolution of MY 34 GDS is still not fully understood. In this study, these two aspects are investigated using MarsPCM simulations. We study seasonal, latitudinal and local time variations in the bulges during nominal dust conditions using MarsPCM simulations prescribed with a "climatology" dust scenario. We present the effect of MY 34 GDS by conducting an independent assessment of simulations from the MarsPCM and MGITM models and study He bulges for pre, peak, and decay phases of the storm.

We find that during a typical Mars year without a GDS, the MarsPCM captures the observed seasonal, latitudinal, and diurnal features of the He bulges more effectively than the MGITM simulations presented in Gupta et al. (2021) and Elrod et al. (2017). However, the predicted densities at mid-to-high latitudes on the nightside are slightly underestimated, whereas those on the dayside are overestimated. In addition, the MarsPCM simulation reveals a larger latitudinal extent of He bulges compared to the locations reported in previous studies for a typical Martian year. The winter bulges during the solstices are shifted toward the winter poles, covering latitudes between 45° and 90°. The bulges are also extended to all the local times at latitudes >75° in the winter hemisphere. During equinoxes, the bulges extend to most of the latitudes on the nightside regions of Mars. Particularly, the southern hemisphere bulges are stronger and extend toward the south pole, covering 45°–90°S latitudes, and to all the local times at latitudes >85°. This suggests a general trend of poleward expansion for the He bulges throughout a typical Martian year.

One of the interesting results of this study is the observation of helium density enhancement on the nightside at equatorial latitudes in NGIMS data. These enhancements consistently align with MarsPCM results during equinoxes. This confirms the presence of a He bulge at equatorial latitudes during equinoxes. This aspect of the He bulge was not evident in MGITM simulations carried out by Gupta et al. (2021) and Elrod et al. (2017). In addition, the latitudinal spread of the He bulges in each season varies with LT. During NSS, the southern winter He bulge exhibits a larger latitudinal extent during 0–8 hr LT compared to their coverage during 18–24 hr LT. However, during NWS, the northern winter bulge expanded more during 18–24 hr LT compared to 0–8 hr LT. The northern winter bulge is also found to be weaker in strength than its southern counterpart. Moreover, He bulges during the first half of the Martian year are stronger than during the second half.

For the MY 34 GDS, our study demonstrates that the poleward shift of the helium bulges is a seasonal feature, as a similar poleward expansion is also observed under nominal dusty conditions. In addition, Simulations from MarsPCM and MGITM show that during the pre-storm phase, the nightside He bulges began to decrease in density while maintaining a well-defined shape. The maximum density decrease occurred during the peak phase of the storm. Additionally, the bulge became significantly distorted and exhibited a clear scattering toward the dayside of Mars. During the decay phase, the He bulge returned to its nominal distribution pattern. This dayside retention of helium during the storm's peak phase is apparent in both model simulations. However, MGITM simulated nightside densities are at least two orders higher than the MarsPCM simulations. On the other hand, the opposite is observed on the dayside. The dust storms on Mars tend to be more frequent and severe during the southern summer (Montabone et al., 2015, 2020). We propose that a weaker zonal winds in the southern summer hemisphere compared to the northern counterpart might contribute to reduced day-to-night transport of helium, resulting in less pronounced He bulges on the nightside. To confirm this hypothesis, a thorough analysis of wind patterns throughout the Martian year is necessary. We tried to follow this approach by analyzing MarsPCM
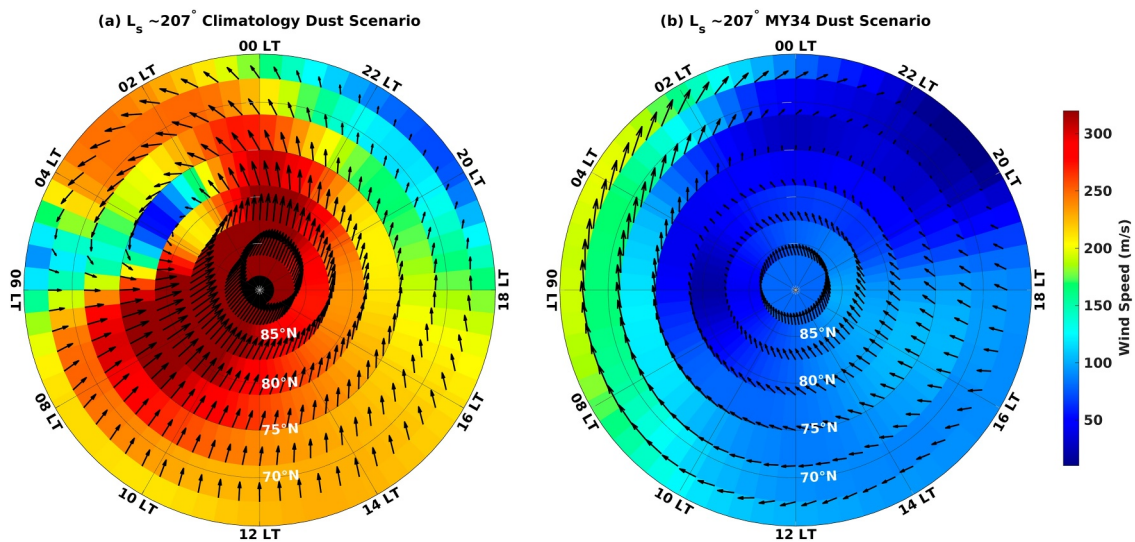
Figure 8. Polar stereographic projected horizontal wind vectors (arrows) superimposed onto wind magnitude (shading) at 1.38×10^{-6} Pa in the northern hemisphere for the MarsPCM simulations with (a) "climatology" and (b) "MY 34" dust scenario for $L_s \sim 207°$ (representing peak phase of the GDS). Here, the x axis represents the LT in hrs and the y axis represents the latitude.

simulated winds with the "MY 34" dust scenario as a case study. MY 34, being a global dust storm year, resembles a condition similar to the typical dusty second half of the year but with a significantly higher dust loading.

Figure 8 presents MarsPCM simulations of horizontal wind patterns under two dust scenarios: the "climatology" scenario and the "MY 34" scenario, both corresponding to the peak phase of the GDS. In the climatology scenario (Figure 8a), high-latitude (>70°N) winds reach ~320 m/s. The circulation between 6–16 hr LT is dominated by a meridional wind component, facilitating poleward transport of the He bulge from the dayside to the nightside regions of Mars. In contrast, the "MY 34" dust scenario (Figure 8b) shows significantly reduced wind magnitudes on the dayside, particularly between 6–16 hr LT, approximately four times weaker than the climatology scenario. The meridional component is also diminished between 70°N and 80°N during 6–16 hr LT. Instead, a dominant zonal wind component is observed, directed from west to east. While a weak meridional component remains at latitudes above 80°N, the overall strength of the day-to-night circulation is substantially reduced. This weak circulation during the MY 34 dust storm likely contributed to the observed dayside retention of the He bulge and the distorted nightside bulge. Moreover, the weak atmospheric circulation during the second half of the Martian year is likely responsible for the lower He bulge density compared with the first half.

During a GDS on Mars, the thermospheric circulation experiences significant dampening due to a combination of thermal and dynamic processes. The intense absorption of solar radiation by suspended dust particles leads to strong infrared heating in the lower and middle atmospheres, which in turn warms these layers and reduces the vertical temperature gradient between the lower atmosphere and the thermosphere (Guha & Panda, 2021, 2022; Heavens et al., 2019; Kass et al., 2020; Keating et al., 1998; Vlasov et al., 2022). This diminished gradient weakens vertical coupling and lessens the efficiency of upward energy transfer. Simultaneously, enhanced infrared cooling by CO_2 in the upper atmosphere, especially at night and in the winter hemisphere, leads to a reduction in thermospheric temperatures and pressure gradients, further weakening global-scale winds (Bougher et al., 2023; Medvedev et al., 2015; Gonzalez-Galindo et al., 2013). In addition, the altered background wind and temperature fields during a GDS disrupt the propagation of gravity and planetary waves, resulting in reduced wave-driven momentum and energy deposition in the thermosphere (Elrod et al., 2023; Liu et al., 2023; Medvedev et al., 2011, 2013; Roeten et al., 2022). These changes collectively contribute to the weakening of day-to-night circulation, diminished meridional transport, and stagnation of thermospheric flows. Ultimately, this dampens overall dynamical activity in the upper atmosphere, leading to the retention of the He bulge on the dayside of Mars.

It is important to understand the factors that govern the thermal and dynamical structure, which is crucial for reconciling the differences observed between MarsPCM and MGITM simulations. Both models are whole-

atmosphere general circulation models, spanning from the surface to the exosphere (∼0–250 km). However, they are intrinsically different in their design and parameterizations. MarsPCM is an extension of the terrestrial LMDZ model with Mars-specific physical parameterizations (González-Galindo et al., 2009, 2013; 2015). In contrast, MGITM is based on the terrestrial GITM framework, combining elements from NASA Ames MGCM and NCAR MTGCM (Bougher et al., 2015). One of the key differences relevant to this study lies in how each model handles the processes involved in the dust parameterization. MarsPCM employs a semi-interactive dust setup (Madeleine et al., 2011), where active dust lifting is constrained by a prescribed column dust optical depth, yielding a prognostic vertical distribution by taking care of the dust moments, dust radiation, lifting, transport, sedimentation, and scavenging. This approach enables interactive radiative heating profiles, incorporating feedback from temperature and dynamics. This setup is crucial for isolating the effect of dust radiative feedback on the atmospheric circulation and its subsequent impact on the atmospheric tracers, such as Helium. On the other hand, MGITM uses a prescribed column dust optical depth and a zonally averaged vertical dust distribution (assuming it is well mixed zonally), along with precomputed heating rates to force the model (Bougher et al., 2015). Notably, the dust in MGITM can be set in the same way as that in MarsPCM. However, at present, it has no real-time radiative calculation; thus, dust heating is static and decoupled from the atmospheric variability. Consequently, its influence on temperature and circulation is limited to predefined dust and heating profiles, with no dynamic feedback. These differences in the treatment of dust and radiative feedback are expected to produce noticeable discrepancies in the model outputs, particularly under dusty atmospheric conditions.

Additionally, MGITM incorporates a GW parameterization scheme that extends up to the exosphere, allowing the model to capture gravity wave effects at very high altitudes (Roeten et al., 2022). However, the current GW scheme in MGITM is static (Roeten et al., 2022). It does not include seasonal variability in the launching height of the wave spectrum (at the top of the planetary boundary layer) and uses constant GW parameters. This lack of spatial and temporal variability can lead to overestimated He densities, particularly in the nightside high-latitude regions of Mars (Elrod et al., 2023). Consequently, studies of the He bulges under nominal dusty conditions and the multiple phases of GDS using MGITM simulation are subject to biases. In contrast, MarsPCM sets the wave launching level at a sigma pressure level ∼250pa, which varies with location and season (Gilli et al., 2020), allowing for more spatially variable GW effects. Comparisons between simulations with and without the GW parameterization have already demonstrated the significant impact of GWs on shaping the global wind patterns and thermal structure of the upper atmosphere (Elrod et al., 2023; Liu et al., 2023; Medvedev et al., 2011, 2013; Roeten et al., 2022). These effects become even more pronounced under dust storm conditions, which alter global circulation patterns and influence GW propagation and dissipation, feeding back into the dynamics (Elrod et al., 2023; Medvedev et al., 2013). Although these differences do not fully account for the discrepancies in He bulge densities between MarsPCM and MGITM, it is evident that dust conditions and gravity waves play a critical role in the formation and evolution of He bulges throughout the Martian year, including during dust storms. Despite differences in their parameterization, both models predict similar spatial and temporal patterns of the He bulges and their response to the MY 34 GDS, suggesting that these features are largely model-independent. Nonetheless, the combined effects of the differing GW and dust parameterizations may account for the remaining discrepancies between the two models.

It is worth reminding that the simulations in this study were performed using MarsPCM version 5, and the results show good agreement with those from MGITM. Recent developments in MarsPCM include updates to the dust cycle (Millour et al., 2024; Wang et al., 2018) and gravity wave (GW) parameterizations (Liu et al., 2023, 2025). In version 6, the dust cycle combines three key parameterizations: realistic injection constrained by daily scenarios, rocket dust storms, and mountain-top flows. Unlike version 5, which applied strict daily renormalization, version six employs a modest radiative adjustment, allowing dust to evolve more freely with the dynamics. However, these updates produce negligible effects on the upper atmosphere during the first half of the Martian year at pressures below 2 Pa, though some hot biases appear in the second half (Bierjon et al., 2022). The hot bias from high dust loading could be reduced by incorporating dust–gas non-local thermal equilibrium above 40 km, although the dust updates in version 6 seem to have only a limited impact on the upper atmosphere (Goldenson et al., 2008; Haberle et al., 2022).

Additionally, the GW scheme in version six extends to 250 km (Liu et al., 2023, 2025), compared to 120 km in version 5 (Gilli et al., 2020), and is governed by seven tunable parameters. While most values remain similar between versions, The GW parameterization constants in version 5 were not adjusted to Mars during the development, which has been fixed in version 6 (Liu et al., 2023, 2025). For example, differences include the GW

launch level, which is fixed at a constant pressure in version 5 but tied to the planetary boundary height in version 6. Both schemes dampen upper atmospheric winds though version 6 produces stronger effects along with upper atmospheric cooling. At the time this work was initiated, the version six improvements had not been fully validated or publicly released, making version 5 the more established and reliable choice. Nonetheless, incorporating version 6 could refine the upper atmospheric response, which may be a potential future scope of this study.

6. Summary

In this study, the seasonal, latitudinal, and local time characteristics of He bulges, under nominal dust conditions, are investigated using MAVEN NGIMS observations from MY 32 to 37, supported by MarsPCM simulations. MarsPCM shows significantly better agreement with NGIMS observations than model simulations used in previous studies (Elrod et al., 2017; Gupta et al., 2021). While MarsPCM simulated bulge densities are slightly underestimated on the nightside regions of Mars, they are overestimated on the dayside. However, the locations of the He bulges are well captured in the model simulations for all seasons. In addition, the impact of the MY 34 GDS on these bulges is examined using MarsPCM and further complemented by simulations from MGITM. We focus on isolating the specific effects of the MY 34 GDS by analyzing simulations from both models during the pre-, peak-, and post-storm phases. The results of the study show that during the GDS, upper atmospheric circulation weakens, causing shifts in the location of He bulges with respect to both local time and latitude. Overall, the findings of this study strongly suggest a correlation between the He bulge formation and the dynamic structure of the Martian upper atmosphere.

During equinoxes, NGIMS observations show that helium densities are enhanced at equatorial latitudes (30°N–30°S) during 0–8 hr and 20–24 hr LT. Additionally, some signatures in the NGIMS data suggest an influence of large dust storms on the formation or modification of He bulges. During solstices, the NGIMS data set confirms that the northern winter bulge is nearly 10 times weaker than its southern counterpart. These observations are compared with "climatology" simulations from MarsPCM. The equatorial He density enhancement observed during equinoxes is consistent with MarsPCM simulations, which indicate the presence of a nightside equatorial He bulge in addition to the one observed at mid-to-high latitudes. This equatorial bulge was not captured in the MGITM simulations carried out by Gupta et al. (2021). Furthermore, MarsPCM simulations show that the southern mid-to-high latitude bulge extends across a broad latitudinal range, from ~45°N to 90°S, between 0 and 8 hr and 18–24 hr LT. This bulge exhibits a poleward extension in the southern hemisphere, which was not captured previously by MGITM simulations, and was identified as an anomalous feature of the bulges in Gupta et al. (2021) and Elrod et al. (2017). Additionally, southern hemisphere bulges are stronger than their northern counterparts during equinoxes.

For solstices, MarsPCM simulations confirm the asymmetry in the strength of the winter bulges. Thus, the seasonal variations in He bulge strength observed in the NGIMS data are well aligned with MarsPCM predictions. In contrast, MGITM simulations predicted nearly uniform He bulge strength throughout the Martian year. Moreover, MarsPCM predicted that winter bulges have a larger latitudinal extend and are situated farther poleward, persisting across all local times at latitudes greater than 75° in the winter hemisphere. Also, poleward displaced bulges during solstices and equinoxes are observed throughout the Martian year and are inherent to the formation mechanism.

MarsPCM simulations reveal that the seasonal migration of He bulges begins around $L_s \sim 50°$, shifting from the northern to the southern winter hemisphere, and around $L_s \sim 183°$, returning from the southern to the northern winter hemisphere, an aspect not previously quantified. The latitudinal extent of the winter bulges also varies seasonally and diurnally; it is larger during 0–8 hr LT in the first half of the year and during 18–24 hr LT in the second half. Additionally, the bulges are stronger during the first half of the Martian year at all local times.

During the MY 34 GDS, the He bulge exhibited slight changes in the pre-storm phase. However, a substantial reduction in bulge density and a dispersal of the bulge toward the dayside of Mars occurred during the peak phase, indicating a strong impact of the GDS. Subsequently, the He bulge gradually returned to its seasonal norm during the decay phase of the storm. The changes are apparent in the simulations from both the MarsPCM and MGITM models. During the peak phase, a substantial decrease in the magnitude of dayside meridional winds relative to the "climatology" dust scenario is observed in MarsPCM simulations. This weakening of the meridional circulation causes He bulge to remain confined to the dayside. The plausible mechanism responsible for this dampening is the

alteration of the thermal and dynamical structure of the upper atmosphere. These alterations are likely caused by reduction in vertical transport of energy, changes in radiative cooling, and energy and momentum deposition by gravity waves. These effects collectively reduce the day-to-night transport of helium, thereby explaining the observed dayside retention of the He bulge. These findings represent a significant contribution to advancing model development and improving our understanding of the Martian upper atmosphere.

Conflict of Interest

The authors declare no conflicts of interest relevant to this study.

Data Availability Statement

All the NGIMS/MAVEN data (L2: V08_R01) used here are publicly available at the MAVEN Science Data Center website (https://atmos.nmsu.edu/PDS/data/PDS4/MAVEN/ngims_bundle/). The MarsPCM used in this work can be downloaded from the SVN repository at https://svn.lmd.jussieu.fr/Planeto/trunk/LMDZ.MARS/. More information and documentation are available at http://www-planets.lmd.jussieu.fr and https://lmdz-forge.lmd.jussieu.fr/mediawiki/Planets/index.php/Overview_of_the_Mars_PCM. The MarsPCM simulations used in this study are archived in the Mendeley Data Repository (Gupta, 2025). The column dust optical depth maps (Montabone et al., 2015, 2020) used to run MarsPCM with "climatology" dust scenario are publicly available on the Mars Climate Database (Forget et al., 1999; Millour et al., 2018) project webpage at https://www-mars.lmd.jussieu.fr/mars/dust_climatology/ in NetCDF format, and on the Europlanet VESPA repository (https://vespa.obspm.fr/ then search for Mars dust – Mars airborne dust) in FITS format. The MGITM simulations used in this study are archived on the university of Michigan Deep Blue Data repository (Bougher, 2025; Roeten & Bougher, 2022).

References

Aldhaheri, S., Gupta, N., & Gebhardt, C. (2024). Effects of regional storms on helium densities realized through MPCM simulations and EMM observation for Martian year 36. *LPI Contributions*, *3007*, 3102. https://www.hou.usra.edu/meetings/tenthmars2024/pdf/3102.pdf

Angelats i Coll, M., Forget, F., López-Valverde, M., & González-Galindo, F. (2005). The first Mars thermospheric general circulation model: The Martian atmosphere from the ground to 240 km. *Journal of Geophysical Research Letters*, *32*(4), L4201. https://doi.org/10.1029/2004GL021368

Benna, M., & Elrod, M. (2019). NGIMS PDS software interface specification MAVEN-NGIMS-SIS-0001, PDS atmospheres node. Retrieved from https://atmos.nmsu.edu/data_and_services/atmospheres_data/MAVEN/ngims.html

Bierjon, A., Millour, E., & Forget, F. (2022). *Improvement of the PCM version 6–Dust (Deliverable D2.1: Finalization of the GCM version 6–Improving the Dust Cycle; ESA Contract No. 4000128572/19/NL/AS)*. Laboratoire de Météorologie Dynamique. CNRS-IPSL. Retrieved from https://www-mars.lmd.jussieu.fr/esa/contract2020_2022/deliverables/MS3/D2.1_dust_cycle.pdf

Bougher, S., Keating, G., Zurek, R., Murphy, J., Haberle, R., Hollingsworth, J., & Clancy, R. T. (1999). Mars global surveyor aerobraking: Atmospheric trends and model interpretation. *Advances in Space Research*, *23*(11), 1887–1897. https://doi.org/10.1016/S0273-1177(99)00272-0

Bougher, S. W. (2025). Mars thermosphere temperatures, densities and winds: M-GITM simulated datasets for MY33 average dust conditions [Dataset]. *University of Michigan - Deep Blue Data*. https://doi.org/10.7302/bvxq-9e07

Bougher, S. W., Benna, M., Elrod, M., Roeten, K., & Thiemann, E. (2023). MAVEN/NGIMS dayside exospheric temperatures over solar cycle and seasons: Role of dayside thermal balances in regulating temperatures. *Journal of Geophysical Research: Planets*, *128*(1), e2022JE007475. https://doi.org/10.1029/2022JE007475

Bougher, S. W., Engel, S., Roble, R. G., & Foster, B. (2000). Comparative terrestrial planet thermospheres 3. Solar cycle variation of global structure and winds at solstices. *Journal of Geophysical Research*, *105*(E7), 17669–17692. https://doi.org/10.1029/1999JE001232

Bougher, S. W., Pawlowski, D., Bell, J. M., Nelli, S., McDunn, T., Murphy, J. R., et al. (2015). Mars global ionosphere-thermosphere model: Solar cycle, seasonal, and diurnal variations of the Mars upper atmosphere. *Journal of Geophysical Research: Planets*, *120*(2), 311–342. https://doi.org/10.1002/2014JE004715

Bougher, S. W., Roeten, K. J., Olsen, K., Mahaffy, P. R., Benna, M., Elrod, M., et al. (2017). The structure and variability of Mars dayside thermosphere from MAVEN NGIMS and IUVS measurements: Seasonal and solar activity trends in scale heights and temperatures. *Journal of Geophysical Research: Space Physics*, *122*(1), 1296–1313. https://doi.org/10.1002/2016JA023454

Chaufray, J. –Y., Chaffin, M., Deighan, J., Jain, S., Schneider, N., Mayyasi, M., & Jakosky, B. (2020). Effect of the 2018 Martian global dust storm on the CO_2 density in the lower nightside thermosphere observed from MAVEN/IUVS Lyman–alpha absorption. *Geophysical Research Letters*, *47*(7), e2019GL082889. https://doi.org/10.1029/2019GL082889

Colaïtis, A., Spiga, A., Hourdin, F., Rio, C., Forget, F., & Millour, E. (2013). A thermal plume model for the Martian convective boundary layer. *Journal of Geophysical Research: Planets*, *118*(7), 1468–1487. https://doi.org/10.1002/jgre.20104

Elrod, M. K., Bougher, S., Bell, J., Mahaffy, P. R., Benna, M., Stone, S., et al. (2017). He bulge revealed: He and CO_2 diurnal and seasonal variations in the upper atmosphere of Mars as detected by MAVEN NGIMS. *Journal of Geophysical Research: Space Physics*, *122*(2), 2564–2573. https://doi.org/10.1002/2016JA023482

Elrod, M. K., Bougher, S., Roeten, K., & Arnold, K. (2023). Surprising decrease in the Martian He bulge during PEDE-2018 and changes in upper atmospheric circulation. *Journal of Geophysical Research: Planets*, *128*(8), e2022JE007727. https://doi.org/10.1029/2022JE007727

Elrod, M. K., Bougher, S. W., Roeten, K., Sharrar, R., & Murphy, J. (2020). Structural and compositional changes in the upper atmosphere related to the PEDE–2018 dust event on Mars as observed by MAVEN NGIMS. *Geophysical Research Letters*, *47*(4), e2019GL084378. https://doi.org/10.1029/2019GL084378

Farahat, A., Mayyasi, M., Withers, P., Dayeh, M. A., & Abuelgasim, A. (2021). Effects of the June 2018 global dust storm on the atmospheric composition of the Martian upper atmosphere as observed by MAVEN. *Journal of Geophysical Research: Planets*, *126*(10), e2021JE006868. https://doi.org/10.1029/2021JE006868

Farahat, A., Withers, P., Mayyasi, M., & Dayeh, M. A. (2022). Comparison of the effects of regional and global dust storms on the composition of the ionized species of the Martian upper atmosphere using MAVEN. *Remote Sensing*, *14*(11), 2594. https://doi.org/10.3390/rs14112594

Felici, M., Withers, P., Smith, M. D., González-Galindo, F., Oudrhiri, K., & Kahan, D. (2020). MAVEN ROSE observations of the response of the Martian ionosphere to dust storms. *Journal of Geophysical Research: Space Physics*, *125*(6), e2019JA027083. https://doi.org/10.1029/2019JA027083

Forget, F., Hourdin, F., Fournier, R., Hourdin, C., Talagrand, O., Collins, M., et al. (1999). Improved general circulation models of the Martian atmosphere from the surface to above 80 km. *Journal of Geophysical Research*, *104*(E10), 24155–24175. https://doi.org/10.1029/1999JE001025

Forget, F., Millour, E., Bierjon, A., Delavois, A., Fan, S., Lange, L., et al. (2022). Challenges in Mars climate modelling with the LMD Mars global climate model, now called the Mars 'Planetary Climate Model' (PCM). In *7th workshop on Mars atmosphere modelling and observations* (pp. 14–17). Retrieved from https://insu.hal.science/insu-03690056v1/document

Gilli, G., Forget, F., Spiga, A., Navarro, T., Millour, E., Montabone, L., et al. (2020). Impact of gravity waves on the middle atmosphere of Mars: A non-orographic gravity wave parameterization based on global climate modeling and MCS observations. *Journal of Geophysical Research: Planets*, *125*(3), e2018JE005873. https://doi.org/10.1029/2018JE005873

Goldenson, N., Desch, S., & Christensen, P. (2008). Non-equilibrium between dust and gas temperatures in the Mars atmosphere. *Geophysical Research Letters*, *35*(8), L08813. https://doi.org/10.1029/2007GL032907

González-Galindo, F., Chaufray, J.-Y., López-Valverde, M. A., Gilli, G., Forget, F., Leblanc, F., et al. (2013). 3D Martian Ionosphere model: I. The photochemical ionosphere below 180 km. *Journal of Geophysical Research*, *118*, 2105–2123. https://doi.org/10.1002/jgre.20150

González-Galindo, F., Forget, F., López-Valverde, M., & Angelats i Coll, M. (2009). A ground-to-exosphere Martian general circulation model: 2. Atmosphere during solstice conditions—Thermospheric polar warming. *Journal of Geophysical Research*, *114*(E8), E08004. https://doi.org/10.1029/2008JE003277

González-Galindo, F., López-Valverde, M. A., Forget, F., García-Comas, M., Millour, E., & Montabone, L. (2015). Variability of the Martian thermosphere during eight Martian years as simulated by a ground-to-exosphere global circulation model. *Journal of Geophysical Research: Planets*, *120*(11), 2020–2035. https://doi.org/10.1002/2015JE004925

Gu, H., Cui, J., Niu, D.-D., Cao, Y.-T., Wu, X.-S., Li, J., et al. (2020). Neutral heating efficiency in the dayside Martian upper atmosphere. *The Astronomical Journal*, *159*(2), 39. https://doi.org/10.3847/1538-3881/ab5fcc

Guha, B. K., Gebhardt, C., Gupta, N., Young, R., Wolff, M. J., & Montabone, L. (2024). Comprehensive analysis of EMM-EXI dust storm database and data coverage from Martian year 36 to 37. *LPI Contributions*, *3007*, 3104. Retrieved from https://www.hou.usra.edu/meetings/tenthmars2024/eposter/3104.pdf

Guha, B. K., & Panda, J. (2021). Mixing time scales of dustiness and some associated effects at middle atmosphere during the 2018 global dust storm. *Advances in Space Research*, *68*(7), 3037–3051. https://doi.org/10.1016/j.asr.2021.05.030

Guha, B. K., & Panda, J. (2022). Analyzing vertical dust distribution and associated meteorological characteristics over Acidalia Planitia during a regional and global dust event. *Icarus*, *388*, 115230. https://doi.org/10.1016/j.icarus.2022.115230

Gupta, N., Rao, N. V., Bougher, S., & Elrod, M. K. (2021). Latitudinal and seasonal asymmetries of the He bulge in the Martian upper atmosphere. *Journal of Geophysical Research: Planets*, *126*(10), e2021JE006976. https://doi.org/10.1029/2021JE006976

Gupta, N., Sharma, B., Aldhaheri, S., Gebhardt, C., Guha, B. K., Montabone, L., & Young, R. (2024). Climatological analysis of helium bulges in Mars's upper atmosphere using MAVEN and EMM observations and MPCM simulations. *LPI Contributions*, *3007*, 3231. https://www.hou.usra.edu/meetings/tenthmars2024/pdf/3231.pdf

Gupta, N. (2025). Characteristics of helium bulges and the impact of martian year 34 global dust storm using MAVEN/NGIMS observations and MarsPCM and MGITM simulations [Dataset]. *Mendeley, V1*. https://data.mendeley.com/datasets/8y342zxwkd/1

Guzewich, S. D., Fedorova, A. A., Kahre, M. A., & Toigo, A. D. (2020). Studies of the 2018/Mars year 34 planet-encircling dust storm. *Journal of Geophysical Research: Planets*, *125*(12), e2020JE006700. https://doi.org/10.1029/2020JE006700

Haberle, R. M., Hollingsworth, J. L., Colaprete, A., Bridger, A. F. C., McKay, C. P., Murphy, J. R., et al. (2003). The NASA/AMES Mars general circulation model: Model improvements and comparison with observations. In *Mars atmosphere modeling and observations workshop*. Retrieved from https://ntrs.nasa.gov/api/citations/20030018903/downloads/20030018903.pdf

Haberle, R. M., Joshi, M. M., Murphy, J. R., Barnes, J. R., Schofield, J. T., Wilson, G., et al. (1999). General circulation model simulations of the Mars pathfinder atmospheric structure investigation/meteorology data. *Journal of Geophysical Research*, *104*(E4), 8957–8974. https://doi.org/10.1029/1998JE900040

Haberle, R. M., Kahre, M. A., Bertrand, T., Hartwick, V. L., Wilson, R. J., Wolff, M. J., & Batterson, C. (2022). Modeling studies of dust/gas non-thermal equilibrium in the martian atmosphere. In *Seventh international workshop on the Mars atmosphere: Modelling and observations*, (p. 1404)

Heavens, N. G., Kass, D. M., & Shirley, J. H. (2019). Dusty deep convection in the Mars year 34 planet-encircling dust event. *Journal of Geophysical Research: Planets*, *124*(11), 2863–2892. https://doi.org/10.1029/2019je006110

Heavens, N. G., Kleinböhl, A., Chaffin, M. S., Halekas, J. S., Kass, D. M., Hayne, P. O., et al. (2018). Hydrogen escape from Mars enhanced by deep convection in dust storms. *Nature Astronomy*, *2*, 126–132. https://doi.org/10.1038/s41550–017–0353–4

Jain, S., Bougher, S., Deighan, J., Schneider, N., González–Galindo, F., Stewart, A., et al. (2020). Martian thermospheric warming associated with the planet encircling dust event of 2018. *Geophysical Research Letters*, *47*(3), e2019GL085302. https://doi.org/10.1029/2019GL085302

Jakosky, B. M., Grebowsky, J. M., Luhmann, J. G., & Brain, D. A. (2015). Initial results from the MAVEN mission to Mars. *Geophysical Research Letters*, *42*(21), 8791–8802. https://doi.org/10.1002/2015GL065271

Jakosky, B. M., Lin, R. P., Grebowsky, J. M., Luhmann, J. G., Mitchell, D. F., Beutelschies, G., et al. (2015). The Mars atmosphere and volatile evolution (MAVEN) mission. *Space Science Reviews*, *195*(1–4), 3–48. https://doi.org/10.1007/s11214-015-0139-x

Kass, D. M., Schofield, J. T., Kleinböhl, A., McCleese, D. J., Heavens, N. G., Shirley, J. H., & Steele, L. J. (2020). Mars climate sounder observation of Mars' 2018 global dust storm. *Geophysical Research Letters*, *47*(23), e2019GL083931. https://doi.org/10.1029/2019GL083931

Keating, G. M., Bougher, S. W., Zurek, R. W., Tolson, R. H., Cancro, G. J., Noll, S. N., et al. (1998). The structure of the upper atmosphere of Mars: In situ accelerometer measurements from Mars global surveyor. *Science*, *279*(5357), 1672–1676. https://doi.org/10.1126/science.279.5357.1672

Kleinböhl, A., Friedson, A. J., & Schofield, J. T. (2017). Two-dimensional radiative transfer for the retrieval of limb emission measurements in the Martian atmosphere. *Journal of Quantitative Spectroscopy and Radiative Transfer*, *187*, 511–522. https://doi.org/10.1016/j.jqsrt.2016.07.009

Kleinböhl, A., Kass, D. M., Schreier, M., Piqueux, S., Suzuki, S., Shirley, J. H., et al. (2024). Far infrared radiative properties of Mars atmospheric aerosols and their application to Mars climate sounder retrievals of aerosol profiles, aerosol columns and surface temperatures. *Icarus*, *419*, 116000. https://doi.org/10.1016/j.icarus.2024.116000

Kleinböhl, A., Schofield, J. T., Abdou, W. A., Irwin, P. G. J., & de Kok, R. J. (2011). A single-scattering approximation for infrared radiative transfer in limb geometry in the Martian atmosphere. *Journal of Quantitative Spectroscopy & Radiative Transfer*, *112*(10), 1568–1580. https://doi.org/10.1016/j.jqsrt.2011.03.006

Kleinböhl, A., Schofield, J. T., Kass, D. M., Abdou, W. A., Backus, C. R., Sen, B., et al. (2009). Mars climate sounder limb profile retrieval of atmospheric temperature, pressure, and dust and water ice opacity. *Journal of Geophysical Research*, *114*, E10006. https://doi.org/10.1029/2009JE003358

Lange, L., Forget, F., Dupont, E., Vandemeulebrouck, R., Spiga, A., Millour, E., et al. (2023). Modeling slope microclimates in the Mars planetary climate model. *Journal of Geophysical Research: Planets*, *128*(10), e2023JE007915. https://doi.org/10.1029/2023JE007915

Leelavathi, V., Venkateswara, R. N., & Rao, S. (2020). Interannual variability of atmospheric gravity waves in the Martian thermosphere: Effects of the 2018 planet–encircling dust event. *Journal of Geophysical Research: Planets*, *125*(12), e2020JE006649. https://doi.org/10.1029/2020JE006649

Lefèvre, F., Bertaux, J. L., Clancy, R., Encrenaz, T., Fast, K., Forget, F., et al. (2008). Heterogeneous chemistry in the atmosphere of Mars. *Nature*, *454*(7207), 971–975. https://doi.org/10.1038/nature07116

Liu, G., England, S. L., Lillis, R. J., Withers, P., Mahaffy, P. R., Rowland, D. E., et al. (2018). Thermospheric expansion associated with dust increase in the lower atmosphere on Mars observed by MAVEN/NGIMS. *Geophysical Research Letters*, *45*(7), 2901–2910. https://doi.org/10.1002/2018GL077525

Liu, J., Millour, E., Forget, F., Gilli, G., Lott, F., Bardet, D., et al. (2023). A surface to exosphere non-orographic gravity wave parameterization for the Mars planetary climate model. *Journal of Geophysical Research: Planets*, *128*(7), e2023JE007769. https://doi.org/10.1029/2023JE007769

Liu, J., Millour, E., Forget, F., Gilli, G., Lott, F., Bardet, D., & Galindo, F. G. (2025). Diurnal cycle of non-orographic gravity waves' source altitudes and its impacts: Tests with Mars planetary climate model. *Journal of Geophysical Research: Planets*, *130*(7), e2024JE008880. https://doi.org/10.1029/2024JE008880

Liu, X., Wang, W., Thayer, J. P., Burns, A., Sutton, E., Solomon, S. C., et al. (2014). The winter helium bulge revisited. *Geophysical Research Letters*, *41*(19), 6603–6609. https://doi.org/10.1002/2014GL061471

Määttänen, A., Mathé, C., Audouard, J., Listowski, C., Millour, E., Forget, F., et al. (2022). Troposphere-to-mesosphere microphysics of carbon dioxide ice clouds in a Mars global climate model. *Icarus*, *385*, 115098. https://doi.org/10.1016/j.Icarus.2022.115098

Madeleine, J.-B., Forget, F., Millour, E., Montabone, L., & Wolff, M. J. (2011). Revisiting the radiative impact of dust on Mars using the LMD global climate model. *Journal of Geophysical Research*, *116*(E11), E11010. https://doi.org/10.1029/2011JE003855

Mahaffy, P. R., Benna, M., Elrod, M., Yelle, R. V., Bougher, S. W., Stone, S. W., & Jakosky, B. M. (2015). Structure and composition of the neutral upper atmosphere of Mars from the MAVEN NGIMS investigation. *Geophysical Research Letters*, *42*(21), 8951–8957. https://doi.org/10.1002/2015gl065329

Mahaffy, P. R., Benna, M., King, T., Harpold, D. N., Arvey, R., Barciniak, M., et al. (2014). The neutral gas and ion mass spectrometer on the Mars atmosphere and volatile evolution mission. *Space Science Reviews*, *195*(1–4), 49–73. https://doi.org/10.1007/s11214-014-0091-1

Medvedev, A. S., González-Galindo, F., Yiǧit, E., Feofilov, A. G., Forget, F., & Hartogh, P. (2015). Cooling of the Martian thermosphere by CO2 radiation and gravity waves: An inter comparison study with two general circulation models. *Journal of Geophysical Research: Planets*, *120*(5), 913–927. https://doi.org/10.1002/2015JE004802

Medvedev, A. S., Yiǧit, E., Hartogh, P., & Becker, E. (2011). Influence of gravity waves on the Martian atmosphere: General circulation modeling. *Journal of Geophysical Research*, *116*(E10), E10004. https://doi.org/10.1029/2011JE003848

Medvedev, A. S., Yiǧit, E., Kuroda, T., & Hartogh, P. (2013). General circulation modeling of the Martian upper atmosphere during global dust storms. *Journal of Geophysical Research: Planets*, *118*(10), 2234–2246. https://doi.org/10.1002/2013JE004429

Millour, E., Bierjon, A., Forget, F., Spiga, A., Wang, C., & MarsPCM Team (2024). *Improving the vertical distribution of airborne dust in the MarsPCM, tenth international conference on Mars, abstract, 3308, 2024*. Lunar and Planetary Institute. Retrieved from https://www.hou.usra.edu/meetings/tenthmars2024/pdf/3308.pdf

Millour, E., Forget, F., Spiga, A., Vals, M., Zakharov, V., Montabone, L., et al. (2018). The Mars climate database (version 5.3). In *Scientific workshop: From Mars express to ExoMars (27–28 February 2018)*. ESAC.

Montabone, L., Forget, F., Millour, E., Wilson, R., Lewis, S., Cantor, B., et al. (2015). Eight-year climatology of dust optical depth on Mars. *Icarus*, *251*, 65–95. https://doi.org/10.1016/j.Icarus.2014.12.034

Montabone, L., Spiga, A., Kass, D. M., Kleinboehl, A., Forget, F., & Millour, E. (2020). Martian year 34 column dust climatology from Mars climate sounder observations: Reconstructed maps and model simulations. *Journal of Geophysical Research: Planets*, *125*(8), e2019JE006111. https://doi.org/10.1029/2019JE006111

Navarro, T., B Madeleine, J.-, Forget, F., Spiga, A., Millour, E., Montmessin, F., & Määttänen, A. (2014). Global climate modeling of the Martian water cycle with improved microphysics and radiatively active water ice clouds. *Journal of Geophysical Research: Planets*, *119*(7), 1479–1495. https://doi.org/10.1002/2013JE004550

Pottier, A., Forget, F., Montmessin, F., Navarro, T., Spiga, A., Millour, E., et al. (2017). Unraveling the Martian water cycle with high-resolution global climate simulations. *Icarus*, *291*, 82–106. https://doi.org/10.1016/j.Icarus.2017.02.016

Ridley, A., Deng, Y., & Tòth, G. (2006). The global ionosphere-thermosphere model. *Journal of Atmospheric and Solar-Terrestrial Physics*, *68*(8), 839–864. https://doi.org/10.1016/j.jastp.2006.01.008

Roeten, K., & Bougher, S. (2022). MGITM datasets used for a modeling study of the mean impacts of subgrid-scale gravity waves on thermospheric velocities and temperatures at Mars [Dataset]. *University of Michigan—Deep Blue Data*. https://doi.org/10.7302/7hab-2340

Roeten, K. J., Bougher, S. W., Benna, M., & Elrod, M. K. (2022). MAVEN/NGIMS wind observation in the Martian thermosphere during the 2018 planet encircling dust event. *Icarus*, *382*, 115006. https://doi.org/10.1016/j.Icarus.2022.115006

Shaposhnikov, D. S., Medvedev, A. S., Rodin, A. V., Yiǧit, E., & Hartogh, P. (2022). Martian dust storms and gravity waves: Disentangling water transport to the upper atmosphere. *Journal of Geophysical Research: Planets*, *127*(1), 628. https://doi.org/10.1029/2021JE007102

Shirley, J. H., Kleinböhl, A., Kass, D. M., Steele, L. J., Heavens, N. G., Suzuki, S., et al. (2020). Rapid expansion and evolution of a regional dust storm in the Acidalia corridor during the initial growth phase of the Martian global dust storm of 2018. *Geophysical Research Letters*, *47*(9), e2019GL084317. https://doi.org/10.1029/2019GL084317

Smith, M. D. (2019). THEMIS observations of the 2018 Mars global dust storm. *Journal of Geophysical Research: Planets*, *124*(11), 2929–2944. https://doi.org/10.1029/2019JE006107

Stcherbinine, A., Vincendon, M., Montmessin, F., Wolff, M. J., Korablev, O., Fedorova, A., et al. (2020). Martian water ice clouds during the 2018 global dust storm as observed by the ACS-MIR channel onboard the trace gas orbiter. *Journal of Geophysical Research: Planets*, *125*(3), e2019JE006300. https://doi.org/10.1029/2019JE006300

Stone, S. W., Yelle, R. V., Benna, M., Elrod, M. K., & Mahaffy, P. R. (2018). Thermal structure of the Martian upper atmosphere from MA-VEN NGIMS. *Journal of Geophysical Research: Planets*, *123*(11), 2842–2867. https://doi.org/10.1029/2018JE005559

Sun, M., Hao, G., Cui, J., Wu, X., Huang, X., Ni, Y., et al. (2023). Enhanced hydrogen escape on Mars during the 2018 global dust storm: Impact of horizontal wind field. *The Astrophysical Journal*, *953*(1), 71. https://doi.org/10.3847/1538-4357/ace43e

Thiemann, E. M. B., Chamberlin, P. C., Eparvier, F. G., Templeman, B., Woods, T. N., Bougher, S. W., & Jakosky, B. M. (2017). The MAVEN EUVM model of solar spectral irradiance variability at Mars: Algorithms and results. *Journal of Geophysical Research: Space Physics*, *122*(3), 2748–2767. https://doi.org/10.1002/2016JA023512

Vals, M., Rossi, L., Montmessin, F., Lefèvre, F., Gonzalez-Galindo, F., Fedorova, A., et al. (2022). Improved modeling of Mars' HDO cycle using a Mars' global climate model. *Journal of Geophysical Research: Planets*, *127*(8), e2022JE007192. https://doi.org/10.1029/2022JE007192

Venkateswara Rao, N., Gupta, N., & Kadhane, U. R. (2020). Enhanced densities in the Martian thermosphere associated with the 2018 planet-encircling dust event: Results from MENCA/MOM and NGIMS/MAVEN. *Journal of Geophysical Research: Planets*, *125*(10), e2020JE006430. https://doi.org/10.1029/2020JE006430

Vlasov, P., Ignatiev, N., Guerlet, S., Grassi, D., Korablev, O., Grigoriev, A., et al. (2022). Martian atmospheric thermal structure and dust distribution during the MY 34 global dust storm from ACS TIRVIM nadir observations. *Journal of Geophysical Research: Planets*, *127*(9), e2022JE007272. https://doi.org/10.1029/2022je007272

Wang, C., Forget, F., Bertrand, T., Spiga, A., Millour, E., & Navarro, T. (2018). Parameterization of rocket dust storms on Mars in the LMD Martian GCM: Modeling details and validation. *Journal of Geophysical Research: Planets*, *123*(4), 982–1000. https://doi.org/10.1002/2017JE005255

Wolkenberg, P., Giuranna, M., Smith, M. D., Grassi, D., & Amoroso, M. (2020). Similarities and differences of global dust storms in MY 25, 28, and 34. *Journal of Geophysical Research: Planets*, *125*(3), e2019JE006104. https://doi.org/10.1029/2019JE006104

Yiğit, E., Aylward, A. D., & Medvedev, A. S. (2008). Parameterization of the effects of vertically propagating gravity waves for thermosphere general circulation models: Sensitivity study. *Journal of Geophysical Research*, *113*(D19), D19106. https://doi.org/10.1029/2008JD010135

Yiğit, E., Medvedev, A., Benna, M., & Jakosky, B. (2021). Dust storm–enhanced gravity wave activity in the Martian thermosphere observed by MAVEN and implications for atmospheric escape. *Geophysical Research Letters*, *48*(5), e2020GL092095. https://doi.org/10.1029/2020GL092095